The Effect of Co on the Deformation Response of Fe-Mn Alloys

by

Timothy S. Fountain
Submitted to the Department of Materials Science and Engineering and
the Department of Mechanical Engineering in Partial Fulfillment of the Requirements
for the Degrees of

Master of Science in Materials Science and Engineering
and
Naval Engineer

at the Massachusetts Institute of Technology
June 2021

Author……
Department of Materials Science and Engineering
Department of Mechanical Engineering
May 24, 2021

Certified by……
C. Cem Tasan
Thomas B. King Associate Professor of Metallurgy
Thesis Advisor

Certified by……
Tomasz Wierzbicki
Professor of Applied Mechanics
Thesis Reader

Accepted by……..…
Frances M. Ross
Department of Materials Science and Engineering
Chairman, Departmental Committee on Graduate Studies

Accepted by…….....
Nicolas G. Hadjiconstantinou
Department of Mechanical Engineering
Chairman, Departmental Committee on Graduate Studies

THIS PAGE INTENTIONALLY LEFT BLANK

The Effect of Co on the Deformation Response of Fe-Mn Alloys
by
Timothy S. Fountain

Submitted to the Department of Materials Science and Engineering and
the Department of Mechanical Engineering on May 24, 2021,
in Partial Fulfillment of the Requirements for the Degrees of
Master of Science in Materials Science and Engineering and Naval Engineer

Abstract

Fe-Mn alloys are well studied and exhibit several interesting responses to deformation which lead to the possibility of desirable mechanical properties for many engineering applications. The addition of other elements to the system further improves properties and can lead to interesting effects like transformation induced plasticity, twinning induced plasticity, and the shape memory effect. Co is one such alloying agent which has seen use in several alloys which exhibit these behaviors. While Co is known to have an effect on the stacking fault energy of alloys, its precise effect on the Fe-Mn system is somewhat less explored. This study seeks to understand what effect Co has on the Fe-Mn system in terms of its effect on thermodynamic properties, phase composition, deformation induced phase transformation, and mechanical properties. Using a thermodynamic model, three alloys of varying Co concentration with a fixed Fe:Mn ratio of 4 were selected for study to systematically examine the effect that Co has on their response to deformation. An additional alloy of equiatomic composition was created as a basis of comparison. X-ray diffraction, scanning electron microscopy, and microhardness testing were used for evaluation. It is seen that Co has a somewhat complicated effect on the deformation behavior of Fe-Mn alloys. In all alloys, $\gamma \rightarrow \varepsilon$ martensitic transformation occurs. At concentration below 8 at. % Co, increased α' martensite formation within the ε-phase is observed. Possible causes of α' formation within the ε-phase and the effect on microhardness are explored. At concentrations of 8 at. % Co, the ε-phase seems to be stabilized and only $\gamma \rightarrow \alpha'$ transformation is observed. The equiatomic alloy exhibits only $\gamma \rightarrow \varepsilon$ transformation. Several examples of deformation twinning are shown. The thermodynamic model has good agreement with experimental results at low Co concentration, but seems to break down when used for the equiatomic alloy.

THIS PAGE INTENTIONALLY LEFT BLANK

TABLE OF CONTENTS

THIS PAGE INTENTIONALLY LEFT BLANK

Chapter 1

Introduction

The global push to create larger, more technologically advanced navies accentuates the need for sophisticated yet cost-effective shipbuilding materials. Advanced materials offer the possibility for superior survivability while also reducing the weight of similarly sized structures. Modern technology and theoretical modeling offer materials scientists the ability to design materials with exciting properties in a virtually unlimited tradespace. Carefully developed alloy design procedures can be used to precisely tune the properties of these materials and generate large amounts of data quickly and with minimal material usage. A family of alloys in the Fe-Mn-Co-Cr and associated systems have shown several intriguing metallurgical phenomena including twinning induced plasticity (TWIP), transformation induced plasticity (TRIP), and a multi-stage sequential TRIP phenomenon [1-11]. Such responses result in materials with good strength-ductility synergy, enhanced strain hardening effects, and improved fatigue resistance. It is suspected that Co plays a key role in determining the deformation response in these alloys and this study aimed to systematically examine those effects when added to the Fe-Mn system.

The nature of a metal's deformation response can be predicted using its thermodynamic properties. In alloys with a face centered cubic crystal structure, stacking fault energy (SFE) is a thermodynamic property which plays a key role in the determination of that alloy's response to deformation [12,13]. A stacking fault is a planar defect which affects the stacking sequence of atoms in a crystalline material. As a result of the close relationship between the FCC crystal structure and the hexagonal close packed (HCP) crystal structure, the SFE is important in predicting deformation induced transformation behavior. Mn acts as a stabilizing agent for the FCC γ-phase, so the SFE is a good indicator of the deformation response of Fe-Mn alloys. With low SFE, martensitic transformation from $\gamma \rightarrow \varepsilon$ occurs, and as it raises twinning and dislocation slip become dominant [13]. The martensitic transformation of FCC γ-phase to the HCP ε-phase is well documented in literature [12-16] and has significant relevance to several engineering applications [1]. Additionally, the body centered tetragonal BCT α' phase can form from both parent phases [14,15,17-21], further lending to a complicated microstructural environment that warrants further exploration.

Co is suspected to have a strong effect on the magnetic properties of a material which in turn affect the thermodynamic properties which ultimately affect mechanical performance [16]. Co is linked to low SFE materials where beneficial deformation responses are observed [2,4,7,8,16]. However, its effect alone is somewhat limited as much of the literature regarding its addition to Fe-Mn containing alloys is written about HEAs. Experimental data regarding the ternary system is likewise scarce [22,23]. This study seeks to remedy some of those deficiencies in the literature.

First, a thermodynamic model was used to calculate SFEs over a wide range of material composition to predict which alloys may yield deformation response mechanisms of interest. These results were used to select four alloys for study. Those alloys were then produced in an electric arc furnace and all data was collected using only approximately 240 grams of raw

elements. Samples were homogenized and subjected to various degrees of plastic deformation through cold rolling. Chemical homogeneity and overall chemical composition were evaluated using energy dispersive spectroscopy (EDS). Microhardness indentations were made in each processing condition and the deformation response in the vicinity of the indentations was observed under the scanning electron microscope (SEM). Scattered electron (SE), backscattered electron (BSE), and electron backscattered diffraction (EBSD) methods were utilized to observe local deformation responses with high resolution. As-homogenized samples were subjected to cold rolling to 20% and 40% reduction in thickness and the change in bulk phase constitution was measured using an X-ray diffraction (XRD) method. Microhardness measurements were taken in all conditions to screen the mechanical performance. All observed results are compared with initial thermodynamic predictions.

Chapter 2

Experimental Procedures

2.1 Alloy Design

This study explored the effect of Co on the deformation behavior of the Fe-Mn system. Four alloys were produced, thermomechanically processed, and examined following deformation events. Microstructural evolution during deformation was analyzed using a combination of XRD and SEM methods. Hardness measurements were taken to evaluate the mechanical properties experienced resulting from varying degrees of deformation.

The systems of interest develop their distinctive deformation responses in part from their dual phase γ and ε microstructure. These alloys exhibit effects such as TRIP, TWIP, and several pieces of literature report a unique sequential TRIP effect in which secondary transformation yields a non-brittle microstructure following deformation [1,2,4-7]. Therefore, systems with thermodynamic conditions where both γ and ε phases have similar thermal and mechanical stability was desired.

It is documented in the literature that binary Fe-Mn alloys with Mn content between 15 and 28 at. % produce a microstructure comprised of a mixture of γ-austenite and ε-martensite [14]. Alloys with Mn compositions of 20 at. % lead to the highest ultimate tensile strength (UTS) of approximately 785 MPa because at this chemical composition their microstructure has the highest ε-martensite concentration. Raising the Mn content beyond this level lowers strength as the FCC γ-phase becomes dominant [14]. Stress-induced formation of the α' phase within the ε-phase is also apparent with Mn concentrations below 20 at. % [15]. Below Mn compositions of 15 at. %, the γ-phase loses stability and the α' and ε martensite phases dominate in the as-cooled, undeformed condition [14].

Because of the favorable combination of phase constitution and strength found in the binary system at 20 at. % Mn, it was elected to maintain the 4:1 Fe to Mn ratio in the alloys produced for study. Co was added systematically to alloys with this same base ratio and its effects observed. The addition of Co can alter the thermodynamic condition of the alloy and is known to have an impact on the stacking fault energy, an important parameter in predicting which deformation mechanisms are preferred [13,16]. One equiatomic sample was also produced as a basis for comparison to the other alloys.

The procedures utilized to produce and analyze the materials used in this study are detailed here and the theory behind each method of analysis is described.

2.1.1 Alloy Production

Alloys were produced by melting their pure elements of at least 99.9% atomic purity in an electric arc furnace under an Ar environment of 700 $mbar$ absolute pressure. A spherical Ti oxygen getter was melted by the electric arc prior to the raw material to scavenge any remaining oxygen after Ar flushing. Raw materials were placed in a Cu crucible and subjected to 5 successive melts to ensure complete melting and coalescence. Between each melt, the alloy was flipped using a sample manipulator built into the arc melter to ensure uniform melting on both sides of the alloy. The resulting button was then temporarily removed from the machine and the Cu crucible replaced with a Cu mold to perform a suction casting. Figure 2.1 shows the arc melter used in this study for alloy production.

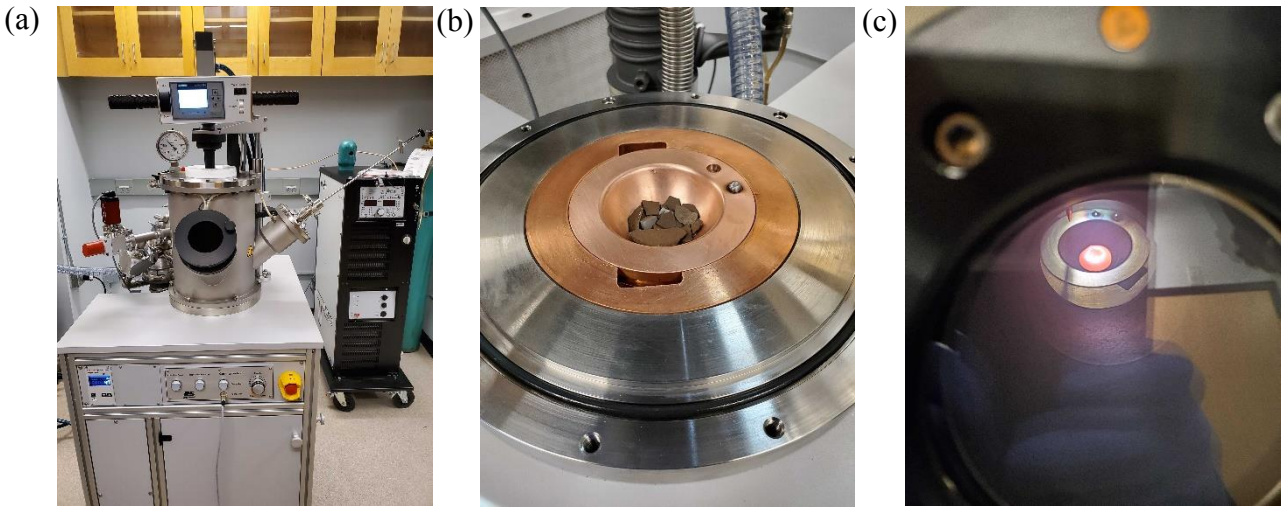

Figure 2.1: *(a):* Arc melter. Sample manipulator can be seen at right of image. *(b):* Raw elements in water-cooled Cu crucible. *(c):* Alloy button as seen through chamber viewport prior to melting of raw material. Spherical Ti oxygen getter can be seen at approximately 12 o'clock to the sample.

The button from the initial melt was placed in the upper portion of the Cu mold in the same manner as the raw materials were placed in the Cu crucible. A channel leading from the upper to lower portion of the mold provided a flow path for the liquid metal into the mold chamber. A pressure differential between the melting chamber and high vacuum tanks of the arc melter was established to provide a driving force for the liquid alloy to be drawn into the mold. The melting chamber was held at 700 $mbar$ absolute pressure of Ar and the high vacuum tanks pumped to 5×10^{-5} $mbar$ absolute pressure. The button was then remelted and a flow path opened between the Ar environment and the high vacuum chambers, causing the liquid metal to be forced into the inner mold to form a casting. The casting was then removed and prepared for sampling. Figure 2.2 shows an example of an alloy in the water-cooled Cu mold after suction casting.

Samples were cut from the casting using electrical discharge machining (EDM) to avoid any plastic deformation or thermal effects on the microstructure.

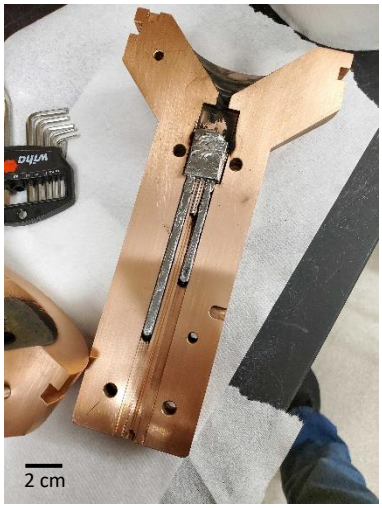

Figure 2.2: Alloy in water-cooled Cu mold after suction casting.

2.1.2 Alloy Chemistry and Energy Dispersive Spectroscopy

Each alloy was assigned a nominal composition and the mass of the raw elements measured to the fourth decimal place prior to melting. The chemistry was then measured and verified through energy dispersive spectroscopy (EDS).

EDS is used to determine the chemistry of a sample through the generation of characteristic X-rays from an incident electron beam. The incident electron ejects an inner shell electron of atoms within the sample, leaving a hole. Since lower energy levels must be filled before higher energy levels, an outer shell electron falls to fill the hole left from the interaction. The difference in energy between the outer shell electron's initial energy state and final energy state is released as an X-ray of specific energy unique to the element it was ejected from. A schematic of this process is shown in Figure 2.3. A detector counts the number of X-rays of specific energies generated and is able to quantify chemical composition in this way. The beam is scanned over the sample to collect data.

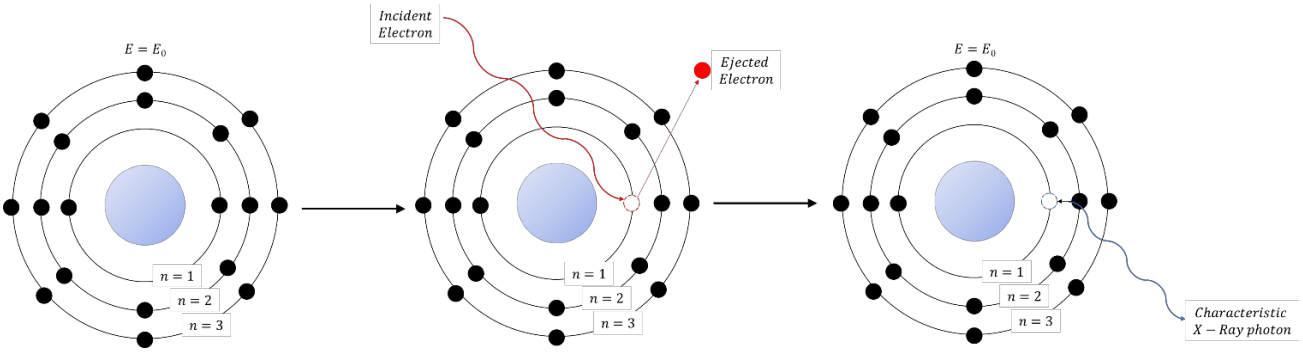

Figure 2.3: Schematic of the principle of EDS. A ground state atom is bombarded by an incident electron beam, ejecting an inner shell electron. A higher energy electron fills the hole left by the ejected inner shell electron, releasing characteristic X-ray radiation in the process.

EDS chemical composition analysis was conducted in a TESCAN MIRA 3 scanning electron microscope (SEM) equipped with EDAX software. The operation voltage was set at 20 kV and the working distance at 15 mm. Line scans were performed with 500 points taken over 100 μm for each sample condition.

The designation of each alloy produced and their nominal compositions are tabulated in Table 2.1. Scans were completed in the as-cast and homogenized conditions to evaluate the effectiveness of the homogenization treatment.

Table 2.1: Nominal chemical compositions of each alloy given in At. %.

	Nominal (At. %)		
Designation	Fe	Mn	Co
$Fe_{80}Mn_{20}$	80	20	0
$Fe_{33}Mn_{33}Co_{33}$	33	33	33
$(FeMn)_{98}Co_2$	79	19	2
$(FeMn)_{95}Co_5$	76	19	5

It should be noted that several difficulties were encountered during the production of the alloy designated $(FeMn)_{98}Co_2$. First, a fire started during the casting process as a result of residue left behind by the highly volatile Mn evaporating in the electric arc melter chamber. During cleaning of the chamber, cleaning media with Mn residue on it combusted in a trashcan prior to suction casting. All samples from this alloy were then taken from the button rather than a cast billet. Second, during homogenization the quartz tube in which the alloy was sealed failed to hold a vacuum and the sample experienced considerable oxidation and burn off of Mn, thus raising the Co concentration much higher than intended. It was elected to keep the alloy with the higher Co percentage as another point of data. The results of each EDS chemistry scan are discussed in Chapter 4.1.

2.1.3 Alloy Homogenization

A thermomechanical processing treatment schedule was developed to homogenize the alloy and refine its grain structure. Materials were first subjected to cold rolling with a 40 % reduction in area (% RA) and were then homogenized at 1000℃ for 4 hours. It was found using the one axis equilibrium plots generated by Thermocalc software and shown in Figure 2.4 that at approximately 900℃ the alloys should be completely in the FCC phase. The diagram for each alloy is similar at high temperatures so for the sake of brevity only one is shown. It was elected to raise homogenization temperature to speed up processing times and was limited to 1000℃ based on the limitations of available furnace equipment. All samples were sealed in a quartz tube and held at vacuum while undergoing thermal treatment.

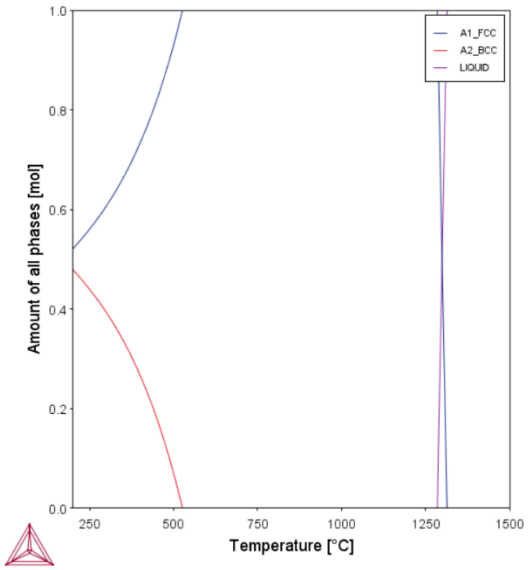

Figure 2.4: Single axis equilibrium diagram generated from Thermocalc software for the $(FeMn)_{98}Co_2$ composition.

2.2 Microstructural Characterization

The microstructure of each alloy was analyzed on the local and global scales using a combination of scanning electron microscopy and X-ray diffraction (XRD). Secondary electron imaging (SEI) and backscattered electron imaging (BSEI) was used to observe surface topography of samples under varying degrees of deformation. Electron backscattered diffraction (EBSD) provided insight into phase composition and crystallographic texture in localized regions and near specific deformation events. Bulk (global) phase characterization of samples in each condition and information inherent to the crystal lattice was obtained using X-ray diffraction for all samples.

Samples were prepared by grinding their surfaces with successively finer particles until a mirror finish was achieved. First, each specimen was mounted in a low temperature, fast curing

acrylic resin to aid in handling of thin specimens during surface preparation. Grinding media was placed on a rotating surface and samples pressed upon them to initiate removal of material.

Surface preparation began with the use of silicon carbide (SiC) particles adhered to paper to mechanically grind away surface imperfections. The following sequence of particle sizes, given in American grit size and European P-grade in parentheses, was used to prepare the samples for fine polishing:

1. 320 grit (P400)
2. 400 grit (P800)
3. 600 grit (P1200)
4. 800 grit (P2400)

Samples were held against each grinding paper until all surface scratches were visually evaluated as having approximately equal depth and direction.

Fine polishing was completed using colloidal diamond suspension with the following particle size and times:

1. 9 μm for 9 minutes
2. 3 μm for 15 minutes
3. 1 μm for 18 minutes

Final polishing was completed using a suspension of colloidal Silica (SiO) particles of 0.05 μm diameter for 36 minutes.

2.2.1 Scanning Electron Microscopy

The SEM provides a versatile means of material characterization by taking advantage of the interactions of an accelerated electron beam with matter. Different interaction methods provide their unique advantages to imaging. Two of these methods, SEI and BSE, were used for microstructural evaluation in this study. These methods are described here.

1. Secondary Electron Imaging. In scanning electron microscopy, secondary electrons are used to analyze the topography of a sample. An incident electron beam inelastically interacts with outer shell electrons near to the surface of the sample, ejecting them. These electrons are then collected on a detector and used to create an image of the surface of the sample [24]. A graphical representation of the formation of an SE is shown in Figure 2.5.

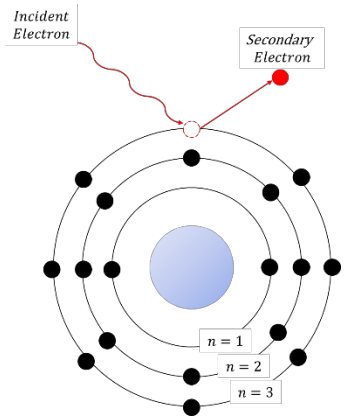

Figure 2.5: Formation of a secondary electron.

2. Backscattered Electron Imaging. Backscattered electrons also provide information about the topography of a sample surface but provide additional insight into different phases and crystallographic orientation. Electrons generated through this method can originate from much deeper in the sample and have higher energy than scattered electrons. Incident electrons interact with the nucleus of an atom and are elastically scattered from the sample. Larger nuclei have a stronger effect on the incident beam and regions with these atoms appear darker on the images produced. Crystallographic orientation also impacts the intensity of the signal received by the detector, and therefore grains of similar composition but different crystallographic orientation can be differentiated from each other [24]. A graphical representation of the generation of a BSE is shown in Figure 2.6.

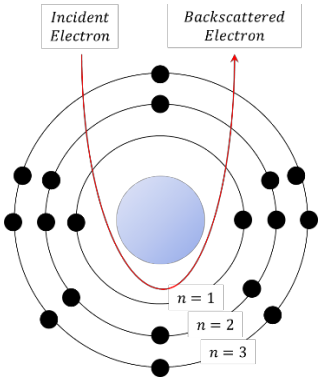

Figure 2.6: Generation of a backscattered electron.

SEM imaging using SEs and BSEs was used for basic imaging of sample surfaces and provided insight into the microstructural characteristics of the samples. All SEM imaging was performed in a TESCAN MIRA 3 SEM with a low-energy BSE (LE-BSE) scintillation detector. For basic imaging, working distance was set at 10 mm and beam voltage set at 20 kV.

2.2.2 Electron Backscattered Diffraction

Electron backscattered diffraction (EBSD) is a technique used for the analysis of phase composition and crystallographic orientations in a sample. The sample is tilted to 70° and bombarded by an incident electron beam. These electrons are back scattered from the sample and the high angle tilt results in more of these electrons reaching a detector, producing a stronger signal. The diffracted electrons form patterns unique to a specific crystal structure and orientation called Kikuchi bands. To raise the intensity of these patterns, and therefore the quality of the image, it is desired for the backscattered waves to interact constructively with each other. Constructive interference is strongest when the wavelength of the radiation and the interplanar spacing of the crystal is similar. The condition where constructive interference is at its strongest can be described by Bragg's Law, shown in equation (2.1).

$$2d \sin(\theta) = n\lambda \quad \textbf{(2.1)}$$

Where d is the interplanar spacing, θ is the glancing angle, n is a positive integer, and λ is the wavelength of the incident radiation wave. The patterns produced can then be analyzed using computer software [24].

In this study a TESCAN MIRA 3 SEM with EBSD hardware was used. Working distance was set to 18 mm with a working voltage of 20 kV. EDAX software with the orientation imaging microscopy (OIM) version 8 software was used to analyze all EBSD results.

2.2.3 X-Ray Diffraction

XRD is a tool used for the analysis of crystallographic information regarding a material. In this study, it is used for phase identification and the determination of important size parameters of the crystals in the alloys produced [25].

Characteristic X-rays are produced by an anode material that is struck by electrons. Incident electrons excite the electrons in the anode material, and these electrons deexcite either through their ejection, known as Auger electrons, or by emitting a characteristic X-ray with an energy unique to the element used in the anode. The characteristic X-rays are filtered such that only a monochromatic beam interacts with the sample. As with electrons in the EBSD technique, the interaction of the X-rays with the sample can be described using Bragg's Law shown in equation (2.1). The diffracted beams produce a pattern on a detector which can be analyzed to obtain information regarding the crystal structure of the material [25].

In this study, a Co anode with a 1.79 Å wavelength was used to eliminate issues with fluorescence experienced in samples containing Fe or Co when a traditional Cu anode is used. Reducing fluorescence likewise reduces background interference. A Bruker D8 machine equipped with GADDS software was used for data collection. Raw data was compiled by plotting intensity (# of interactions) vs. a specific 2θ angle using DiffracEva software developed by Bruker, and

Rietveld refinement of the data was completed using HighScorePlus software developed by Panalytical. An R_{wp} value of less than 8% was used as the basis for successful fitting and was confirmed for each scan.

2.3 Mechanical Testing

The practical goal in producing an alloy is obtaining a material with desirable properties. The elusive combination of high strength and high ductility is a constant effort of materials scientists. Measurement of mechanical properties is necessary for complete characterization of the alloys produced. To this end, microhardness tests were utilized.

2.3.1 Microhardness Testing

Hardness testing measures the resistance of a material to local deformation by pressing a hard indenter into the surface of a sample and measuring the size of the indent produced. A harder material will experience smaller indentation than a softer material. Though several hardness scales and indenters exist, this study utilized the Vickers scale. These tests are performed using a square based, pyramidal diamond indenter pressed into the material at a specified force for a specified time. An angle of 22° (or 136° between the faces of the indenter) between normal to the sample and both sides of the indenter ensures that hardness measurements remain constant regardless of the load used. The depth and surface area of the indentation are measured optically to determine a hardness value. Typically, several indentations are taken within the same material and the average hardness and standard deviation reported to account for and describe material variability. To avoid subsequent measurements being impacted by the effects of work hardening from previous indentations, each indentation should be at least three indentation diameters apart from each other.

Figure 2.4 graphically demonstrates the operation of a Vickers microhardness measurement.

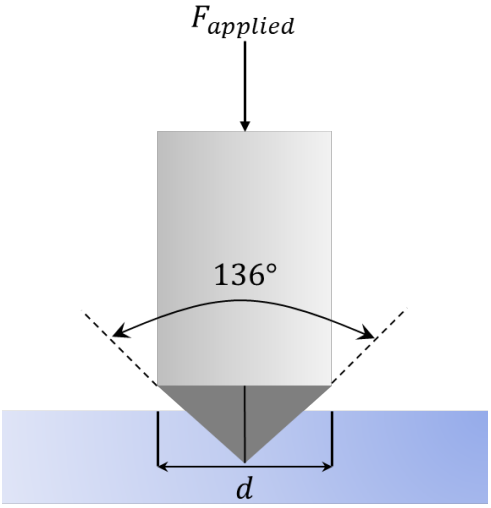

Figure 2.4: Graphical demonstration of a Vickers microhardness test.

Following indentation, an optical microscope is used to observe the indentation and measure its vertical and horizontal diameters. A schematic of the measurements taken is shown in Figure 2.5.

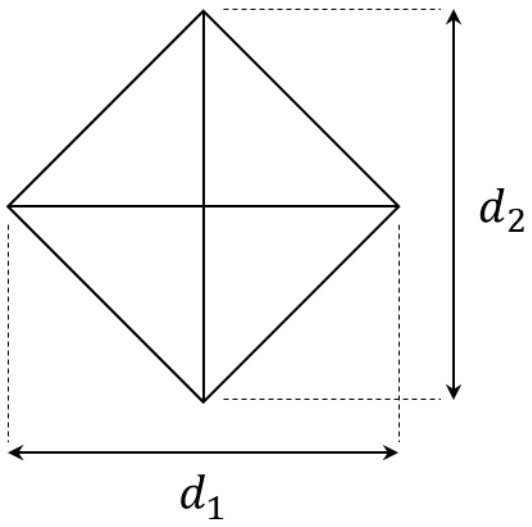

Figure 2.5: Measurements taken of the indentation used in the calculation of Vickers microhardness.

These diameter measurements are taken in units of mm to calculate the surface area of the indentation. The applied load F, measured in kg_f, is then divided by the surface area to obtain the hardness value. Equation (2.2) fully describes the calculation of the Vickers hardness value which is reported as a numeric value in HV.

$$HV = \frac{2Fsin\left(\frac{136°}{2}\right)}{d_1 \times d_2} \quad \textbf{(2.2)}$$

In this study, samples for microhardness testing were prepared according to the methods described in section 2.2. Hardness measurements were performed using a LECO microhardness tester and software with a constant load of 100 g_f with a dwell time of 15 seconds.

Chapter 3

Thermodynamics and Alloy Design

A metal's microstructure, which is dependent upon its chemical composition and processing history, determines its behavior on the macroscopic scale. When appropriately designed, the alloy's thermodynamic condition can be tailored to achieve a desired load-bearing response. The energetics which determine a preferred deformation mechanism are sensitive and therefore a judicious selection of chemical composition is required when exploring new alloys.

The alloys of interest in this study are comprised of three phases. First, ε-martensite is a hard phase with an HCP structure. The second is soft γ-austenite which has a face centered cubic FCC structure. After deformation, some of the alloys also have hard α'-martensite phase which has a BCT structure. Each phase has its own contribution to the overall mechanical performance of the alloy.

It is well established that the close packed FCC and HCP crystal structures are closely related to each other and that FCC → HCP transformation can occur as a result of plastic deformation [12]. The SFE is therefore an important parameter in in determining the preferred deformation mechanism in FCC alloys [13].

In this chapter, a model developed for the calculation of SFE for the Fe-Mn-Co system is discussed and presented as a means of selecting specific alloy compositions that generate a favorable thermodynamic condition for deformation mechanisms which are thought to improve strength-ductility synergy.

3.1 Stacking Faults and Stacking Fault Energy

In a perfect crystal, atoms are arranged in a precise stacking sequence without defects. However, most real crystals inevitably contain defects which disrupt perfect order. These faults are planar defects known as stacking faults and the driving force of their formation is known as stacking fault energy (SFE). A fault in the stacking sequence of an FCC crystal forms an embryo for an HCP crystal, and one of these defects on every alternating (111) plane of FCC crystals yields a bulk HCP structure [12]. A depiction of the FCC and HCP crystal structures and their stacking sequence is shown in Figure 3.1. The FCC structure in 3.1a and 3.1b has a stacking sequence of ABCABC, while the HCP structure in 3.1c and 3.1d has a stacking sequence of ABAB. If the (111) plane in the FCC structure moves from the "c" position to the "a" position (or the "a" to the "c"), a stacking fault is created.

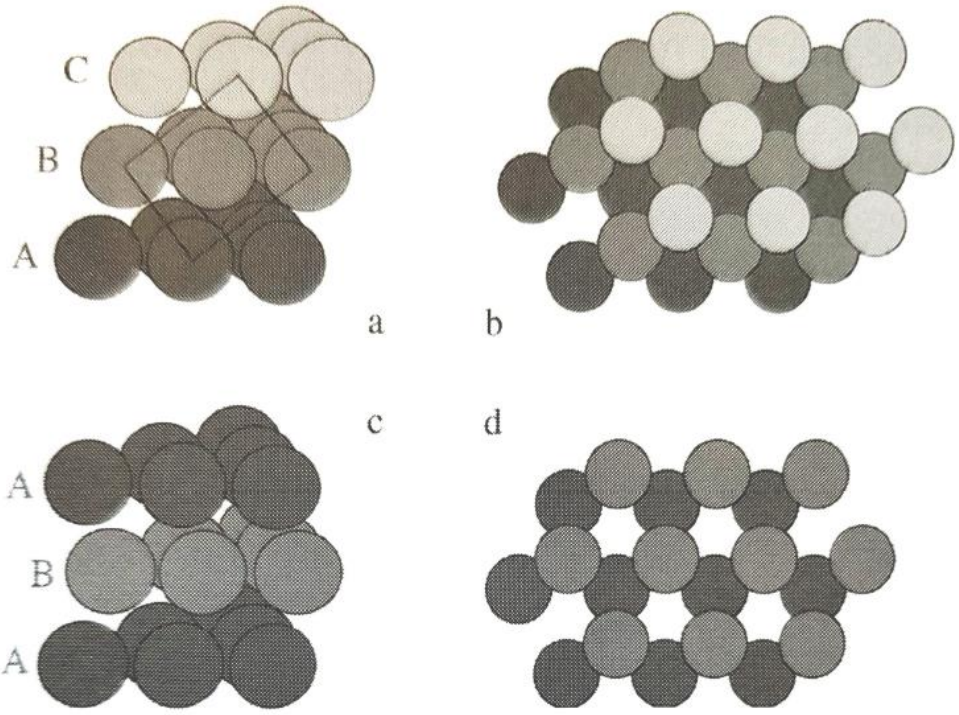

Figure 3.1: Figure taken from *Phase Transitions in Materials* by Brent Fultz [26]. *(a)* ABCABC stacking sequence of (111) planes in an FCC crystal structure. The face of one side of the cubic unit cell is shown for clarity. *(b)* View of 3.1a shown from above. *(c)* HCP crystal structure with ABAB stacking sequence. *(d)* View of 3.1c shown from above.

The SFE is regarded as a critical thermodynamic property that affects the deformation response of an alloy. As shown in Figure 3.2, in the Fe-Mn-Cr-C system SFE's less than about 11 mJ/m^2 result in $\gamma \rightarrow \varepsilon$ transformation, twinning can occur up to about 50 mJ/m^2, and beyond these levels dislocation slip is the dominant mechanism of deformation [13]. A sequential TRIP effect in which a deformation induced phase transformation chain of $\gamma \rightarrow \varepsilon \rightarrow \gamma$ takes place has been reported in the literature with alloys of approximately 6.5 mJ/m^2 [1,2,4-7].

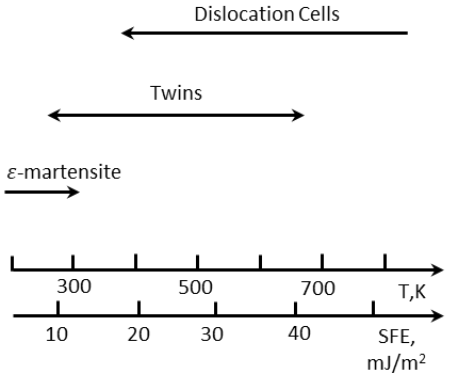

Figure 3.2: Deformation structures as a function of SFE and T [13] for a $Fe_{75.52}Mn_{19.9}Cr_{4.1}C_{0.48}$ alloy.

In this study, deformation induced martensitic transformation (DIMT) and deformation twinning are seen as desirable because of their beneficial impact on mechanical performance [1]. As shown in Figure 3.3, TWIP and TRIP steels excellent strength-ductility synergy compared with other steels. TRIP steels that exhibit a sequential TRIP effect in which a deformation induced phase transformation chain of $\gamma \rightarrow \varepsilon \rightarrow \gamma$ takes place are considered to be especially desirable because they could maintain the benefits of traditional TRIP steels without the resulting embrittlement of a final martensitic microstructure [1,2,4-7]. A low magnitude, positive SFE affords the best opportunity for these effects as it ensures metastable γ-phase in the parent microstructure which can undergo transformation with perturbations from plastic deformation.

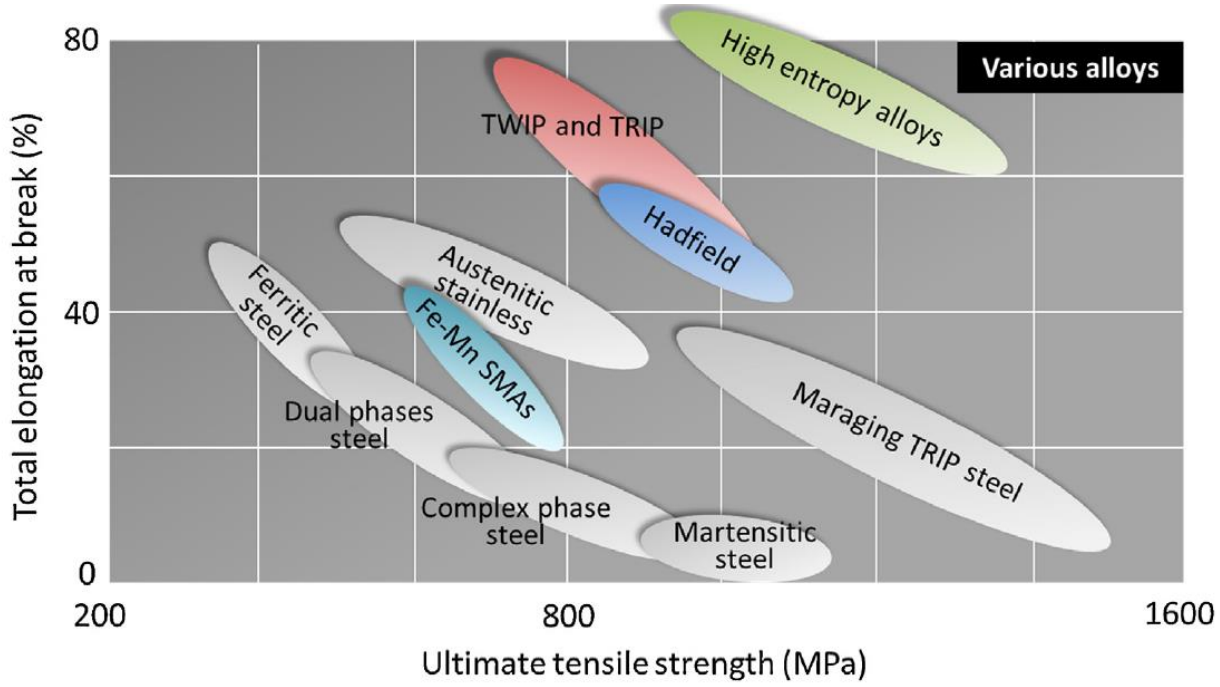

Figure 3.3: Strength-ductility relationships of several types of steels [1].

Therefore, alloys chosen for analysis in this study will be limited to those with small, positive SFE's which fall within or close to the range of SFE's reported as favorable for inducing TRIP, TWIP, or sequential TRIP effects. A thermodynamic model has been produced to predict SFE based on chemical composition and temperature and is described in detail in the next section.

3.2 Thermodynamic Modeling of Stacking Fault Energy

3.2.1 Methodology

SFE can be estimated using a model first proposed by Olson and Cohen in 1976 [12]. The model is based on the number of atomic planes (n), molar surface density (ρ), Gibbs Energy of

transformation ($\Delta G^{\gamma\rightarrow\varepsilon}$) and the interfacial surface energy between the γ and ε phases $\left(\sigma^{\gamma/\varepsilon}\right)$ and is given in equation (3.1).

$$\gamma_{SF} = n\rho\Delta G^{\gamma\rightarrow\varepsilon} + 2\sigma^{\gamma/\varepsilon} \quad \textbf{(3.1)}$$

The parameter n is 2 because it is assumed that the platelet of martensite formed is 2 atomic spacings thick. $\sigma^{\gamma/\varepsilon}$ can be determined directly from literature and is generally given between 5 and 15 mJ/m^2 [2,4,7]. Though disagreement on the value of $\sigma^{\gamma\rightarrow\varepsilon}$ exists [27], 15 mJ/m^2 was chosen for use in this study to maintain consistency with the work of other authors [2,4,7,28].

The value of ρ can be calculated geometrically using the lattice parameter of the alloy using equation (3.2).

$$\rho = \frac{4}{\sqrt{3}\, N_A\, a^2} \quad \textbf{(3.2)}$$

Where N_A is Avogadro's number and a is the lattice parameter. According to measurements of the lattice parameters in the FeMnCo system by Marinelli et. al [29] in 2002, the value of a utilized in this study is 3.6 Å. Therefore, the calculated value of ρ used in this study is $2.96 \times 10^{-5}\,\frac{mol}{m^{-2}}$.

The calculation of $\Delta G^{\gamma\rightarrow\varepsilon}$ was conducted using the regular and subregular solution models. The regular solution model assumes that atoms are distributed randomly in a 3D lattice with no vacancies and calculates the energy of a system by summing the contributions of the unary and binary components to estimate the overall energetics of the ternary system. Unlike the ideal solution model, it adds an excess free energy term to the ideal contribution. The model assumes a non-zero enthalpy of mixing but has no excess entropy. The subregular solution model makes the regular solution model more flexible through its formulation of the excess energy term $\Omega_{ij}^{\gamma\rightarrow\varepsilon}$. A general form of the solution model is given in equation (3.3).

$$\Delta G^{\gamma\rightarrow\varepsilon} = \underbrace{\sum_i X_i\, \Delta G_i^{\gamma\rightarrow\varepsilon}}_{\text{Ideal Contribution}} + \underbrace{\sum_{ij} X_i X_j\, \Omega_{ij}^{\gamma\rightarrow\varepsilon}}_{\text{Excess Contribution}} + \underbrace{\Delta G_{mg}^{\gamma\rightarrow\varepsilon}}_{\text{Magnetic Contribution}} \quad \textbf{(3.3)}$$

X_i is the mole fraction of component i, $\Delta G_i^{\gamma\rightarrow\varepsilon}$ is the ideal Gibbs energy of transformation from the γ to ε phase for component i, $\Delta\Omega_{ij}^{\gamma\rightarrow\varepsilon}$ is the excess free energy contribution from system ij undergoing transformation from γ to ε, and $\Delta G_{mg}^{\gamma\rightarrow\varepsilon}$ is the magnetic free energy term associated with transformation. When applied to the FeMnCo ternary system, equation (3.3) is written as shown in equation (3.4).

$$\Delta G_{rxn}^{\gamma\to\varepsilon} = X_{Fe}\Delta G_{Fe}^{\gamma\to\varepsilon} + X_{Mn}\Delta G_{Mn}^{\gamma\to\varepsilon} + X_{Co}\Delta G_{Co}^{\gamma\to\varepsilon} + X_{Fe}X_{Mn}\Omega_{Fe,Mn}^{\gamma\to\varepsilon} + X_{Fe}X_{Co}\Omega_{Co,Fe}^{\gamma\to\varepsilon} + X_{Co}X_{Mn}\Omega_{Co,Mn}^{\gamma\to\varepsilon} + \Delta G_{m}^{mg,\gamma\to\varepsilon} \quad \textbf{(3.4)}$$

$\Omega_{ij}^{\gamma\to\varepsilon}$ is calculated from two empirical terms, ${}^{0}\mathrm{L}^{\phi}$, which is a linear function of temperature, and ${}^{1}\mathrm{L}^{\phi}$ which is constant. The subregular solution model as shown in equation (3.5) is then used to perform the calculation.

$$\Omega_{ij}^{\gamma\to\varepsilon} = ({}^{0}L^{\varepsilon} - {}^{0}L^{\gamma}) + ({}^{1}L^{\varepsilon} - {}^{1}L^{\gamma})(X_i - X_j) \quad \textbf{(3.5)}$$

The values of $\Delta G_i^{\gamma\to\varepsilon}$, ${}^{0}\mathrm{L}^{\phi}$, ${}^{1}\mathrm{L}^{\phi}$, and the resulting $\Omega_i^{\gamma\to\varepsilon}$ are tabulated in Table 3.1.

Table 3.1: Numerical values and functions used for calculation of equation (2.4).

Parameter	Function (J/mol)	Reference
$\Delta G_{Fe}^{\gamma\to\varepsilon}$	$-821.85 + 1.685T + 0.00222T^2$	[28]
$\Delta G_{Mn}^{\gamma\to\varepsilon}$	$3925 - 2.7T + 0.00455T^2$	[28]
$\Delta G_{Co}^{\gamma\to\varepsilon}$	$-427.59 + 0.615T$	[30]
${}^{0}\mathrm{L}^{\varepsilon}_{\mathrm{FeMn}}$	See result for $\Omega_{Fe,Mn}^{\gamma\to\varepsilon}$	[28]
${}^{0}\mathrm{L}^{\gamma}_{\mathrm{FeMn}}$	See result for $\Omega_{Fe,Mn}^{\gamma\to\varepsilon}$	[28]
${}^{1}\mathrm{L}^{\varepsilon}_{\mathrm{FeMn}}$	See result for $\Omega_{Fe,Mn}^{\gamma\to\varepsilon}$	[28]
${}^{1}\mathrm{L}^{\gamma}_{\mathrm{FeMn}}$	See result for $\Omega_{Fe,Mn}^{\gamma\to\varepsilon}$	[28]
${}^{0}\mathrm{L}^{\varepsilon}_{\mathrm{CoFe}}$	$-8500 + 7T$	[31]
${}^{0}\mathrm{L}^{\gamma}_{\mathrm{CoFe}}$	$-9112 + 3.3T$	[31]
${}^{1}\mathrm{L}^{\varepsilon}_{\mathrm{CoFe}}$	-800	[31]
${}^{2}\mathrm{L}^{\gamma}_{\mathrm{CoFe}}$	1667	[31]
${}^{0}\mathrm{L}^{\varepsilon}_{\mathrm{CoMn}}$	-21000	[32]
${}^{0}\mathrm{L}^{\gamma}_{\mathrm{CoMn}}$	-23756	[32]
${}^{1}\mathrm{L}^{\varepsilon}_{\mathrm{CoMn}}$	-4000	[32]
${}^{1}\mathrm{L}^{\gamma}_{\mathrm{CoMn}}$	-2343	[32]
$\Omega_{Fe,Mn}^{\gamma\to\varepsilon}$	$2180 + 532(X_{Fe} - X_{Mn})$	[28]
$\Omega_{Co,Fe}^{\gamma\to\varepsilon}$	$8341 + (-1181 + 1.6544T)(X_{Co} - X_{Fe})$	[31]
$\Omega_{Co,Mn}^{\gamma\to\varepsilon}$	$2756 - 1657(X_{Co} - X_{Mn})$	[32]

The magnetic contribution to Gibbs energy, $\Delta G_{mg}^{\gamma\to\varepsilon}$, can be calculated using the difference in the values calculated for each phase as shown in equation (3.6).

$$\Delta G_{mg}^{\gamma\to\varepsilon} = \Delta G_{mg}^{\epsilon} - \Delta G_{mg}^{\gamma} \quad \textbf{(3.6)}$$

Calculation of the contribution from each phase can be accomplished by using the model initially proposed by Hillert and Jarl [33] and later refined by Inden [34] (also referred to as the

Inden Hillert-Jarl or IHJ model) shown in equation (3.7). Here, ϕ is used to denote the respective phase, in this case either ε or γ.

$$\Delta G_{mg}^{\phi} = RT * \ln\left(\beta^{\phi} + 1\right) * g^{\phi}(\tau^{\phi}) \tag{3.7}$$

R is the ideal gas constant given as 8.314 J/mol ·K, T is absolute temperature (K), and β^{ϕ} is the magnetic moment of phase ϕ. The function g^{ϕ} is a piecewise polynominal function of τ^{ϕ}, and τ^{ϕ} is the scaled critical magnetic temperature, either the Neèl or Curie temperature. Using the CALPHAD approach, the equation for g^{ϕ} can be calculated from several different models. The original treatment from the IHJ model is given in equation (3.8) [33,34]. The equation for τ^{ϕ} is given in equation (3.9).

$$g(\tau) = \begin{cases} 1 - \frac{1}{A}\left[\frac{79\tau^{-1}}{140p} + \frac{474}{497}\left(\frac{1}{p} - 1\right)\left(\frac{\tau^3}{6} + \frac{\tau^9}{135} + \frac{\tau^{15}}{600}\right)\right], & \tau < 1 \\ -\frac{1}{A}\left(\frac{\tau^{-5}}{10} + \frac{\tau^{-15}}{315} + \frac{\tau^{-25}}{1500}\right), & \tau \geq 1 \end{cases} \tag{3.8}$$

$$\tau^{\phi} = \frac{T}{T_C^{\phi}} \tag{3.9}$$

The parameter A is given as shown in equation (3.10). It is a function of p, the structural factor, and p is equal to 0.28 for both FCC and HCP materials [34].

The IHJ model fails to accurately predict the behavior of antiferromagnetic materials. The critical magnetic temperature can be estimated from experimental data and is a function of chemical composition. When antiferromagnetism is present, the calculated temperature is negative on an absolute temperature scale. In the IHJ model, this issue was dealt with by using an empirically determined "antiferromagnetic factor" first proposed in the 1950s. The factor is -3 for close packed crystal structures (FCC and HCP) and -1 for BCC crystal structures [35]. While this approximation gave reasonable results for the alloys studied during the development of the IHJ model, they are not sufficient for alloys with more complicated magnetic behavior because it introduces artifacts into the data. It was not until 2012 that a new model for the CALPHAD community was developed by Xiong which eliminated these artifacts [36]. In the Xiong model, two Riedlich-Kister polynomials are utilized, one for the Curie and one for the Neèl temperature. Any negative result is set equal to zero as it is assumed that only one stable magnetic transition exists. His model is shown in equation (3.11). Because the ε phase is antiferromagnetic, Xiong's improved magnetic model better captures the behavior of the materials used in the present study and was used in developing the model used for this study.

$$g(\tau) = \begin{cases} 0, & \tau \leq 0 \\ 1 - \frac{1}{D}\left[0.38438376\left(\frac{\tau^{-1}}{p}\right) + 0.63570895\left(\frac{1}{p} - 1\right)\left(\frac{\tau^3}{6} + \frac{\tau^9}{135} + \frac{\tau^{15}}{600} + \frac{\tau^{21}}{1617}\right)\right], & 0 < \tau \leq 1 \\ -\frac{1}{D}\left(\frac{1}{21}\tau^{-7} + \frac{1}{630}\tau^{-21} + \frac{1}{2975}\tau^{-35} + \frac{1}{8232}\tau^{-49}\right), & \tau > 1 \end{cases} \tag{3.11}$$

D is a parameter used in the Xiong model [36] that is a function of p and is analogous to the term A used in the IHJ model. It is shown in equation (3.12).

$$D = 0.33471979 + 0.49649686\left(\frac{1}{p} - 1\right) \tag{3.12}$$

Both β^{ϕ} and T_C^{ϕ} are functions of composition that can be estimated using thermodynamic models. It was elected to use the models developed by Huang [37] for the CALPHAD database because of their relevance to the system of interest and their generally good agreement with experimental data [22]. The functions used in their calculation are tabulated in Table 3.2.

Table 3.2: Functions used for the calculation of magnetic moments and critical magnetic temperatures for the γ and ε phase.

Parameter	Function (units)	Reference
β^{ε}	$1.35X_{Co} - 1.86X_{Mn} + [5.41 - 0.24(X_{Co} - X_{Fe})]X_{Co}X_{Fe}$ $-1.07X_{Co}X_{Mn}$	[37]
β^{γ}	$1.35X_{Co} - 2.1X_{Fe} - 1.86X_{Mn}$ $+[9.74 - 3.516(X_{Co} - X_{Fe})]X_{Co}X_{Fe} - 1.07X_{Co}X_{Mn}$	[37]
T_C^{ε}	$1396X_{Co} - 1620X_{Mn}$ $+[-253 + 1494(X_{Co} - X_{Fe})]X_{Co}X_{Fe}$ $+[-2685 + 3657(X_{Co} - X_{Mn})]X_{Co}X_{Mn}$	[37]
T_C^{γ}	$1396X_{Co} - 201X_{Fe} - 1620X_{Mn}$ $+[283 + 879(X_{Co} - X_{Fe})]X_{Co}X_{Fe}$ $+[-2685 + 3657(X_{Co} - X_{Mn})]X_{Co}X_{Mn}$	[37]

3.2.2 Results

The binary FeMn system was used as a basis for the study and effects on the Gibbs Energy and SFE from Co addition were examined. It was elected to look at the SFE of the binary system with an Fe to Mn ratio of 4:1 and incrementally add Co while maintaining the same ratio as described in 2.1.2. Results from literature seem to suggest that the addition of Co lowers SFE of many alloys [16, 38, 39]. However, as shown in Figure 3.4 for a given Fe to Mn ratio, the model developed for this study predicts that Co has the effect of raising both $\Delta G^{\gamma \to \varepsilon}$ and SFE. Temperatures are given on the absolute scale to correspond with those used in calculations.

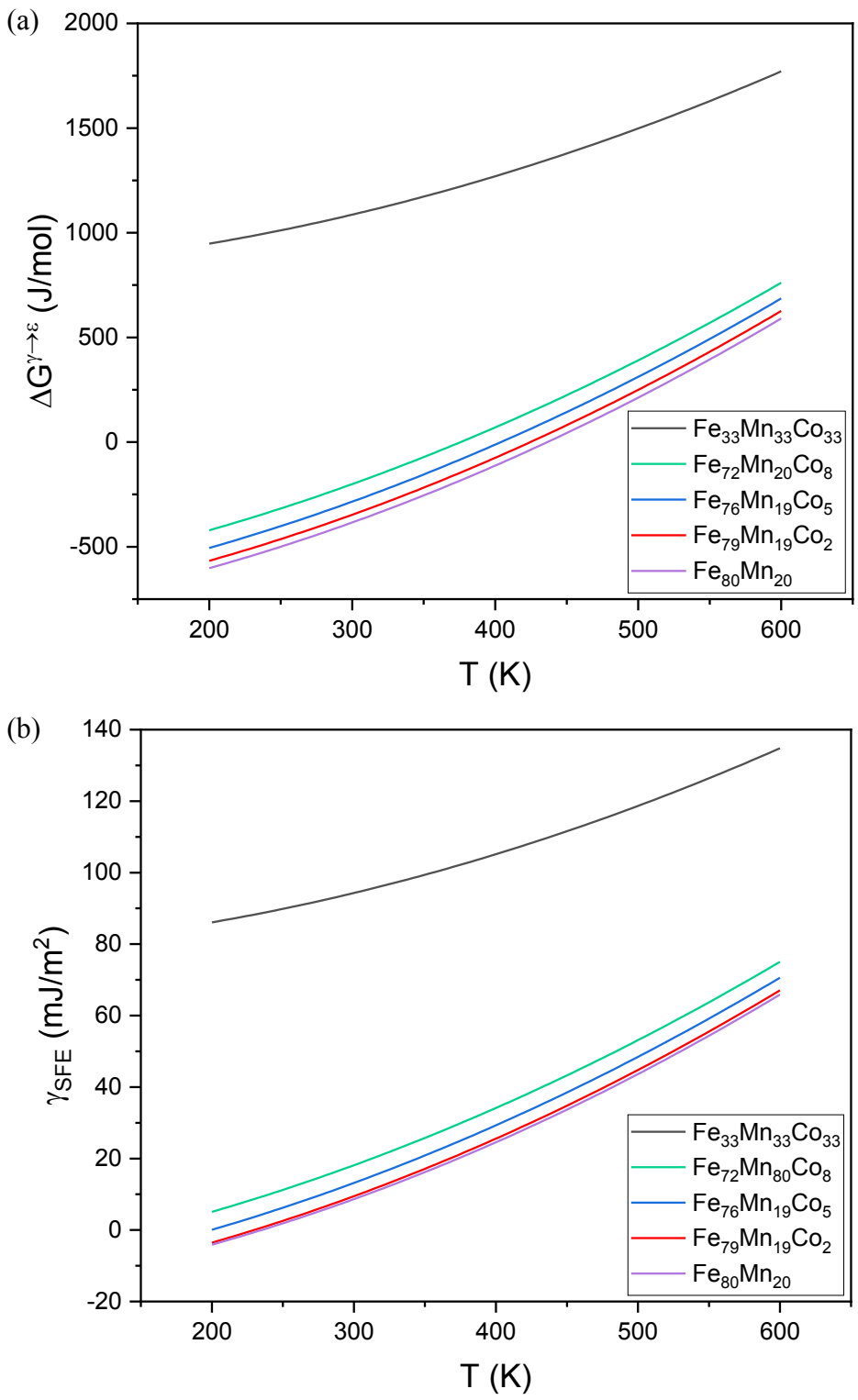

Figure 3.4: *(a):* $\Delta G^{\gamma\rightarrow\varepsilon}$ for each alloy in the study as a function of T. *(b):* γ_{SFE} for each alloy in the study as a function of T.

The SFE for the alloys chosen for study were calculated at 298 K individually and are shown in Table 3.3.

Table 3.3: Alloys selected for analysis and their associated SFEs.

Alloy Composition	SFE (mJ/m^2)
$Fe_{33}Mn_{33}Co_{33}$	94.1
$Fe_{72}Mn_{20}Co_{8}$	18.1
$Fe_{76}Mn_{19}Co_{5}$	12.9
$Fe_{79}Mn_{19}Co_{2}$	9.2
$Fe_{80}Mn_{20}$	7.0

3.2.3 Discussion

With the exception of the equiatomic alloy, each composition has low enough SFE that it should be predicted that some degree of TRIP or TWIP will occur. Higher Co concentration would raise SFE through Co addition, but also could change the Mn content to keep the Fe:Mn ratio of 4 constant.

The raising of SFE through Co addition is surprising given the expected trends from literature. Additionally, Co is expected to be a strong HCP stabilizer based on its equilibrium phase diagram shown in Figure 3.5 [40]. Raising the stability of the HCP phase would therefore be expected to lower SFE as the chemical driving force required to initiate transformation from FCC to HCP structures should lower as well.

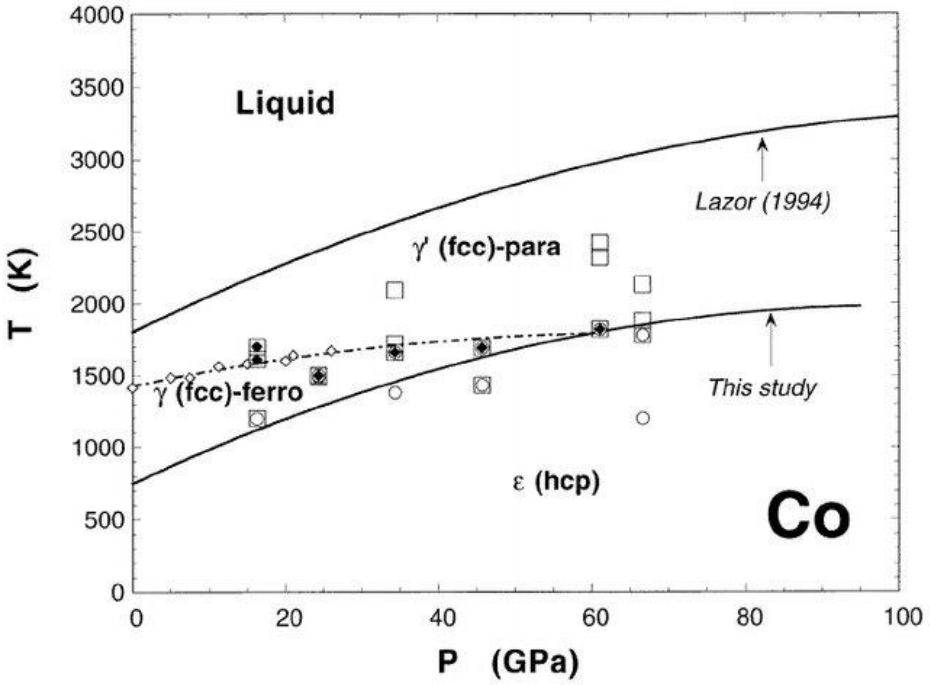

Figure 3.5: Phase diagram for pure Co [40].

The apparent rise in SFE is a result of the effect of Co on T_C^{ϕ}. Contrary to other models [16,38,39], Huang's model predicts that Co raises T_C^{ϕ}, but that T_C^{ϕ} is negative until 37 at. % Co in an alloy with a Mn concentration of approximately 19 at. % as used in this study. In turn, $g(\tau)$ remains 0 according to equation (3.11), eliminating the magnetic contribution to the model. With the magnetic contribution eliminated, the parameters dependent upon Co concentration are the excess free energy contributions. Holding Mn constant while exchanging Fe for Co causes the excess contribution to $\Delta G^{\gamma\rightarrow\varepsilon}$ to rise, thereby raising the SFE. As noted by several authors [41-44], the magnetic models for the Fe-Mn-Co system are inadequate and require refinement. Other authors note difficulties in general with magnetic modeling [36,44,45]. This deficiency could be helped in part by the generation of additional experimental data, as currently, to the best of our knowledge, there are only two articles which provide experimental data on critical magnetic temperatures for the ternary system [22,23].

Results from this thermodynamic study are compared to experimental results in chapter 5.1 and suggestions for future work are given in chapter 5.3.

Chapter 4

Experimental Results

This section will detail the results of all experiments completed throughout the course of this study. EDS was used to verify alloy chemistry and the effectiveness of homogenization treatments. X-Ray diffraction was used for bulk phase composition analysis at varying levels of cold work and to determine the c/a ratio of each alloy. The SEM was used for high resolution imagery of individual deformation events to verify and observe data obtained from XRD and to further characterize the effects of local deformation events using EBSD. Vickers microhardness indents were made as a means of local deformation for SEM analysis. Microhardness measurements were taken to observe the effect that Co has on the strain hardenability of each alloy.

4.1 Energy Dispersive Spectroscopy

An EDS line scan was performed on each alloy in the as-cast and homogenized condition. The chemistry of each point along the line was averaged to obtain an estimate for the overall composition of the alloy. Fluctuations in chemistry across the line were observed to evaluate the effectiveness of the homogenization treatment. Data was smoothed in OriginLab using a Fast Fourier Transform using a low pass filter and 0.625 cut off frequency.

Table 4.1 gives the average of all points across the line to evaluate alloy chemistry of the nominal $Fe_{80}Mn_{20}$ alloy. Overall chemical composition is identical and within an acceptable range of the target composition. Figure 4.1 shows the results of the scan underneath a BSE image of the region in which the scan took place. Though a slightly higher overall deviation is observed in the homogenized sample it appears that there are fewer regions where compositional deviation are present.

Table 4.1: Results of EDS chemistry analysis for $Fe_{80}Mn_{20}$ alloy.

	Fe (At. %)	Mn (At. %)
As-Cast	77.64 ± 1.85	22.36 ± 1.85
Homogenized	77.64 ± 2.00	22.36 ± 2.00

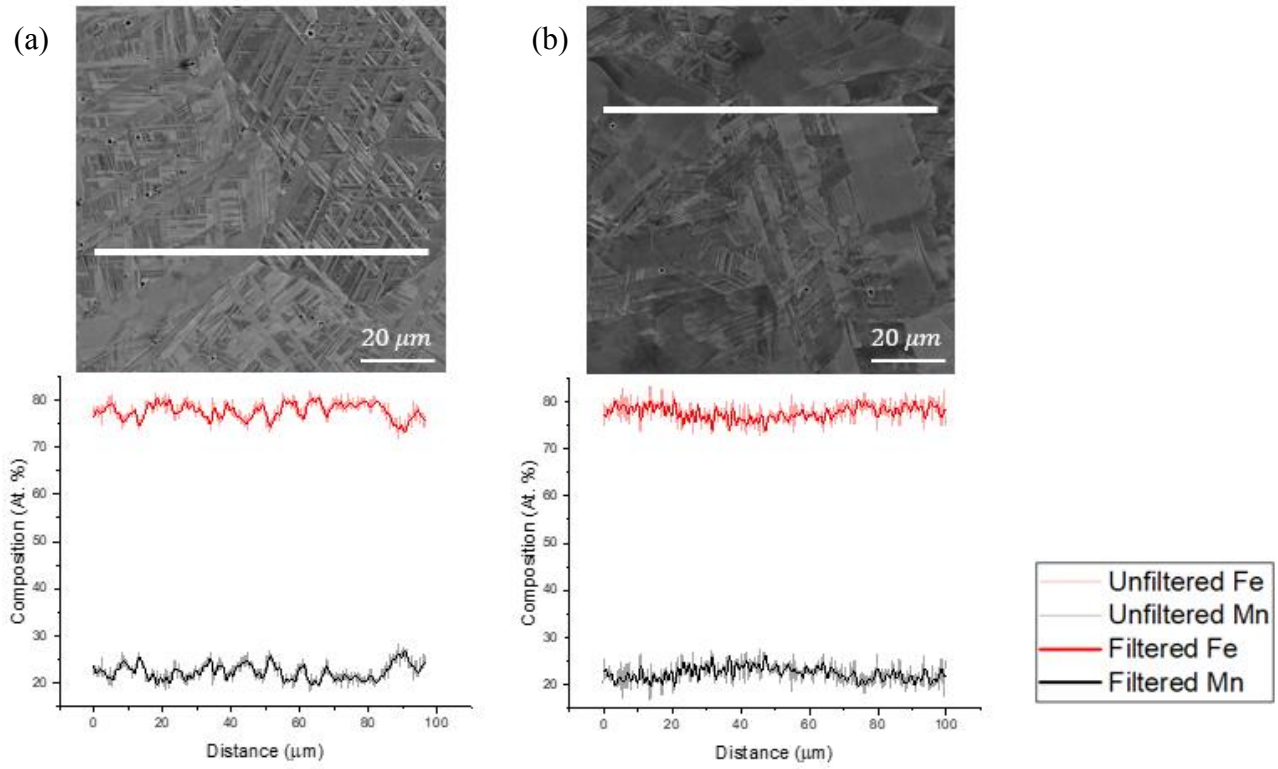

Figure 4.1: BSE image of $Fe_{80}Mn_{20}$ alloy showing location of EDS line scan in the (a) as-cast and (b) homogenized conditions. EDS line scan results for each alloy are shown below their respective BSE image.

Table 4.2 gives the average of all points across the line to evaluate alloy chemistry of the nominal $Fe_{79}Mn_{19}Co_2$ alloy. Figure 4.2 shows the results of the scan underneath a BSE image of the region in which the scan took place. First, the alloy was not suction cast as were the others. This was because during casting a fire broke out in the laboratory as a result of pyrophoric metal powder forming in the chamber of the arc melter. For safety reasons, it was elected to cease production of the alloy until a better procedure was developed. The alloy was therefore left in button form and thus would have experienced a different, slower cooling condition upon casting than the other alloys did. As a result, the microstructure is much blockier than the other alloys. Additionally, during homogenization treatment the quartz tube in which the material was sealed experienced failure and the vacuum was broken. Significant oxidation occurred and as a result some of the Mn in the alloy burned off, resulting in a composition of higher Co than intended. It was elected to keep the alloy and examine it as an 8% Co alloy instead. It will be designated as $Fe_{72}Mn_{20}Co_8$ when analyzed in other sections. Standard deviation of the chemistry across the scan reduced significantly for both Fe and Mn as a result of treatment, however.

Table 4.2: Results of EDS chemistry analysis for nominal $Fe_{79}Mn_{19}Co_2$ alloy.

	Fe (At. %)	Mn (At. %)	Co (At. %)
As-Cast ($Fe_{79}Mn_{20}Co_2$)	72.89 ± 2.08	22.80 ± 1.98	4.31± 0.56
Homogenized ($Fe_{72}Mn_{20}Co_8$)	72.37 ± 1.21	19.62 ± 1.12	8.01 ± 0.79

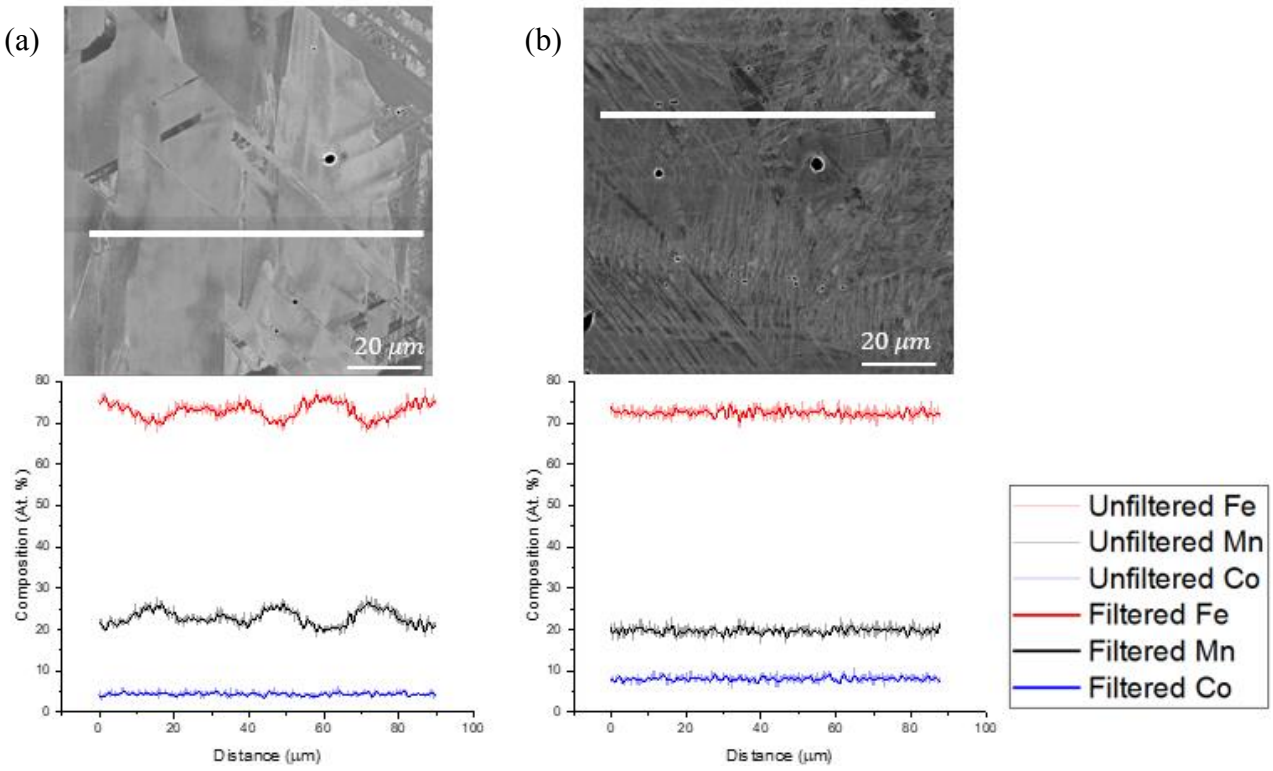

Figure 4.2: BSE image of $Fe_{79}Mn_{19}Co_2$ alloy showing location of EDS line scan in the (a) as-cast and (b) homogenized conditions. EDS line scan results for each alloy are shown below their respective BSE image. Note that in the homogenized condition Mn content dropped and Co content rose as a result of accidental oxidation during heat treatment.

Table 4.3 gives the average of all points across the line to evaluate alloy chemistry of the nominal $Fe_{76}Mn_{19}Co_5$ alloy. Figure 4.3 shows the results of the scan underneath a BSE image of the region in which the scan took place. Overall composition is in an acceptable range of the target composition and standard deviation lowered significantly as a result of homogenization.

Table 4.3: Results of EDS chemistry analysis for nominal $Fe_{76}Mn_{19}Co_5$ alloy.

	Fe (At. %)	Mn (At. %)	Co (At. %)
As-Cast	73.60 ± 2.92	19.41 ± 2.47	6.98 ± 1.20
Homogenized	71.48 ± 1.21	21.16 ± 1.03	7.35 ± 0.67

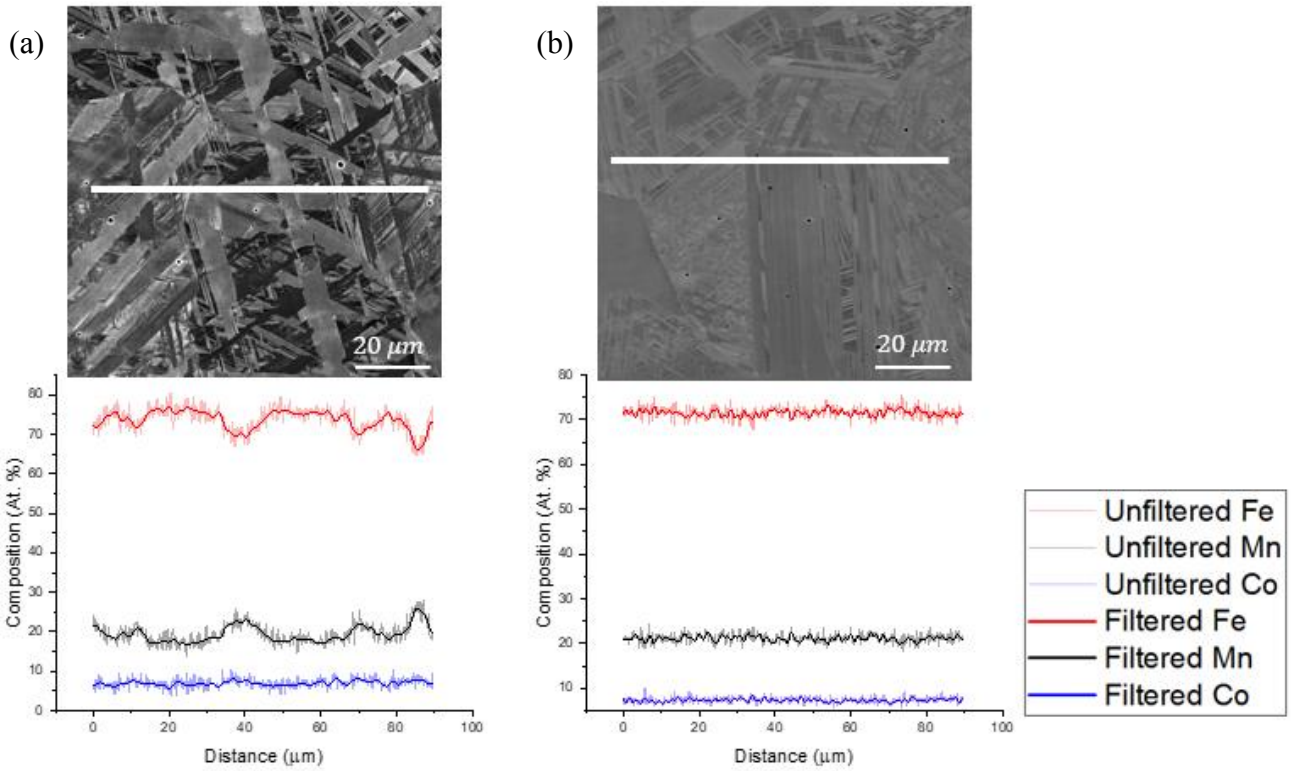

Figure 4.3: BSE image of $Fe_{76}Mn_{19}Co_5$ alloy showing location of EDS line scan in the (a) as-cast and (b) homogenized conditions. EDS line scan results for each alloy are shown below their respective BSE image.

Table 4.4 gives the average of all points across the line to evaluate alloy chemistry of the nominal $Fe_{33}Mn_{33}Co_{33}$ alloy. Overall composition is in an acceptable range of the target composition. Figure 4.4 shows the results of the scan underneath a BSE image of the region in which the scan took place. In the as-cast condition, significant segregation of Mn to interdendritic regions can be observed. This large-scale segregation would likely lead to a significant variation of mechanical properties in localized regions. Homogenization treatment reduced the amount of segregation.

Table 4.4: Results of EDS chemistry analysis for nominal $Fe_{33}Mn_{33}Co_{33}$ alloy.

	Fe (At. %)	Mn (At. %)	Co (At. %)
As-Cast	35.90 ± 3.04	36.78 ± 3.33	27.31 ± 1.09
Homogenized	35.05 ± 1.58	36.56 ± 1.55	28.39 ± 1.29

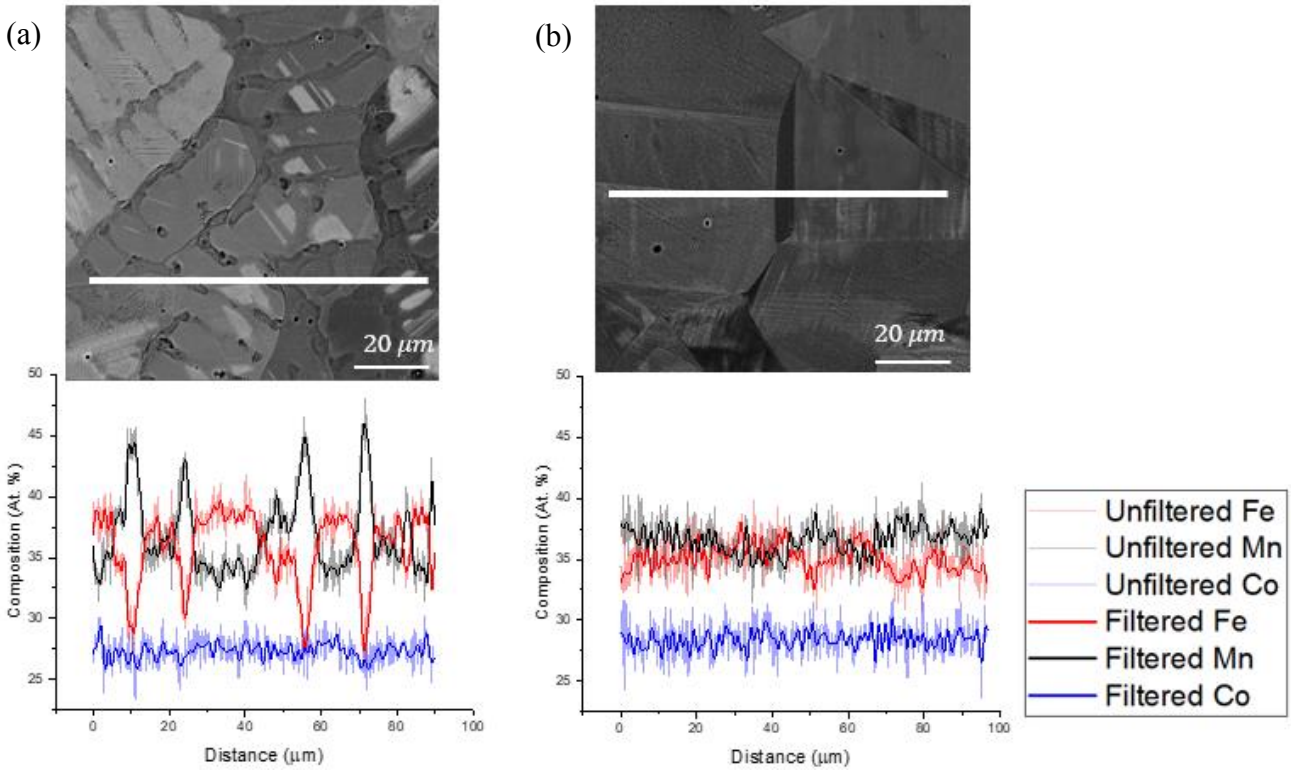

Figure 4.4: BSE image of $Fe_{33}Mn_{33}Co_{33}$ alloy showing location of EDS line scan in the (a) as-cast and (b) homogenized conditions. EDS line scan results for each alloy are shown below their respective BSE image.

A summary of the chemistry of each alloy measured by EDS line scan in each thermal condition is given in Table 4.5.

Table 4.5: Summary of the chemistry of each alloy in the study as measured by EDS line scan.

Alloy	Fe (At. %)	Mn (At. %)	Co (At. %)
$Fe_{80}Mn_{20}$ (As-Cast)	77.64 ± 1.85	22.36 ± 1.85	0
$Fe_{80}Mn_{20}$ (Homogenized)	77.64 ± 2.00	22.36 ± 2.00	0
$Fe_{79}Mn_{19}Co_2$ (As-Cast)	72.89 ± 2.08	22.80 ± 1.98	4.31 ± 0.56
$Fe_{79}Mn_{19}Co_2$ (Homogenized)	72.37 ± 1.21	19.62 ± 1.12	8.01 ± 0.79
$Fe_{76}Mn_{19}Co_5$ (As-Cast)	73.60 ± 2.92	19.41 ± 2.47	6.98 ± 1.20
$Fe_{76}Mn_{19}Co_5$ (Homogenized)	71.48 ± 1.21	21.16 ± 1.03	7.35 ± 0.67
$Fe_{33}Mn_{33}Co_{33}$ (As-Cast)	35.90 ± 3.04	36.78 ± 3.33	27.31 ± 1.09
$Fe_{33}Mn_{33}Co_{33}$ (Homogenized)	35.05 ± 1.58	36.56 ± 1.55	28.39 ± 1.29

4.2 X-Ray Diffraction

XRD was performed as described in Chapter 2.2.3. Results for the c/a ratio are shown for alloys of 0-8% Co concentration in the homogenized condition in Figure 4.5. The result for the equiatomic sample is given in the summary to the right.

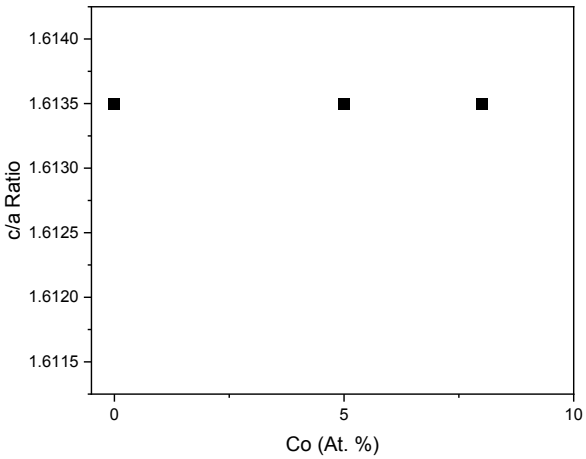

Co (At. %)	c/a Ratio
0	1.61350
5	1.61350
8	1.61350
33	1.61210

Figure 4.5: The c/a ratio given with respect to At. % of Co in each alloy. Numeric values are summarized to the right. Note that the equiatomic sample is not included in the graph.

The measurements indicate that low concentrations of Co added to the Fe-Mn system have no effect on the c/a ratio of the ε phase. The equiatomic sample has a lower c/a ratio, but in both cases the ratio is lower than the ideal c/a ratio of 1.6333 and also beneath $\sqrt{3}$ which can lend insight into twinning behavior should twinning be observed in any of these alloys [46, 47].

Bulk phase composition analysis for each alloy is given in Figure 4.6 in the homogenized condition and also after cold rolling to 20% and 40% reduction in thickness.

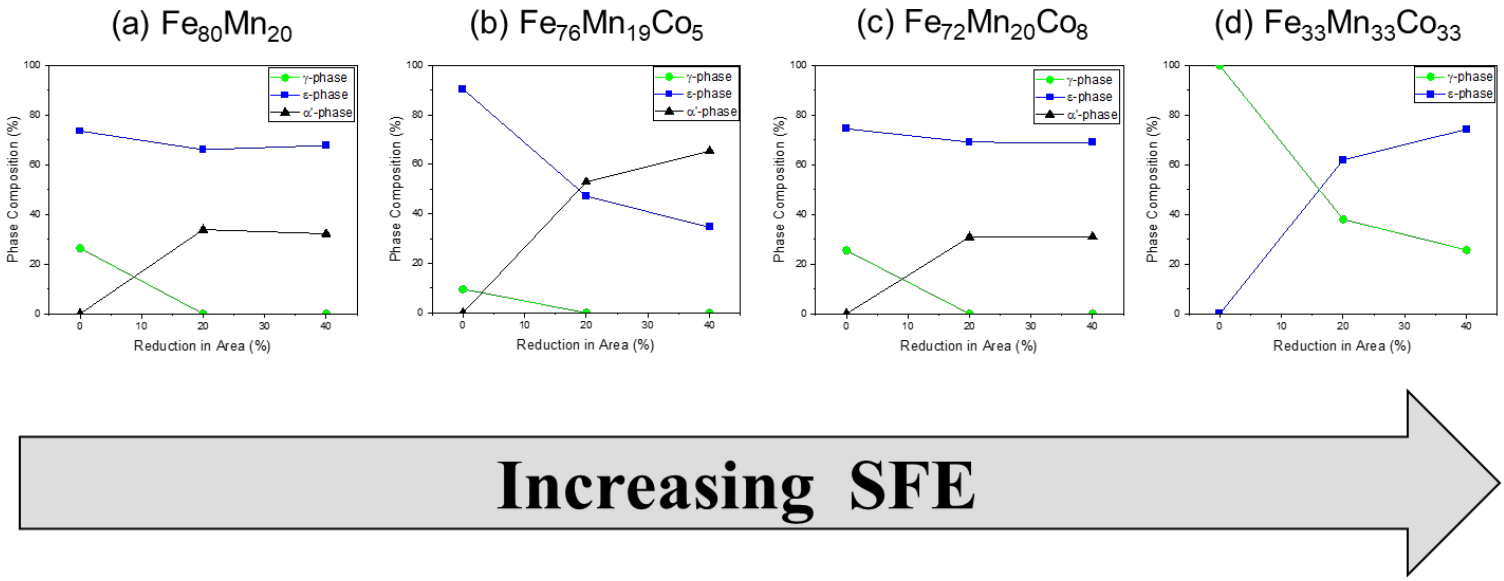

Figure 4.6: Bulk phase composition as a function of reduction in area by cold working measured by XRD for the (a) $Fe_{80}Mn_{20}$, (b) $Fe_{76}Mn_{19}Co_5$, (c) $Fe_{72}Mn_{20}Co_8$, and (d) $Fe_{33}Mn_{33}Co_{33}$ alloys.

The $Fe_{80}Mn_{20}$ alloy shows an initial duplex microstructure of 73.6% ε-phase and 26.4% γ-phase, consistent with expectations for this composition established in the literature [14]. As deformation commences the γ-phase rapidly disappears and the α' phase appears, apparently mostly from the transformation of γ to α'. This transformation is well established in literature [12,14,15,17,18]. However, it should also be noted that ε diminishes initially, indicating some $\varepsilon \rightarrow \alpha'$ transformation as well.

The $Fe_{76}Mn_{19}Co_5$ alloy starts with much higher ε concentration, likely as a result of the stabilizing effect of Co on the HCP structure [40]. The small amount of γ-phase initially present quickly goes to zero, and the reduction is ε phase upon cold working is also notable and occurs at a much higher rate than in the binary system. This observation would indicate that both $\gamma \rightarrow \alpha'$ and $\varepsilon \rightarrow \alpha'$ transformations are occurring but that the addition of Co somehow enhanced this transformation chain. Given that a BCT phase does not exist on the Co phase diagram [40], this result is somewhat surprising but is discussed in greater detail in chapter 5.1.

The most notable feature of the $Fe_{72}Mn_{20}Co_8$ alloy is that there is virtually no change in ε concentration with deformation. All of the γ-phase disappears and α' seems to completely take its place. It should be noted that in addition to higher Co, this alloy had slightly lower Mn content than the 5% Co alloy as measured by EDS. Both of these could contribute to higher ε-phase mechanical stability, making its transformation less likely. This result will be examined in greater detail in chapter 5.1.

The $Fe_{33}Mn_{33}Co_{33}$ alloy has an initial microstructure comprised entirely of γ-phase. As deformation commences, it transforms solely into ε-phase with no evidence of α' formation. This is contradictory to expectations from literature and from the thermodynamic model developed for this study. The result will be examined in greater detail in chapter 5.1.

It is also useful to look at phase constitution vs. % reduction in thickness. The data is presented this way in figure 4.7. With this point of view, it can be seen that ε-phase is reduced for each alloy other than the one of equiatomic composition which increases as the γ-phase undergoes transformation. The $Fe_{76}Mn_{19}Co_5$ alloy shows the greatest reduction in ε, followed by $Fe_{72}Mn_{20}Co_8$, and the binary $Fe_{80}Mn_{20}$ alloy shows the least. In all alloys, the FCC γ-phase is reduced. The $Fe_{33}Mn_{33}Co_{33}$ alloy sees the greatest reduction, but also has the highest amount of initial γ-phase as it is 100% austenitic prior to deformation. The $Fe_{80}Mn_{20}$ and $Fe_{72}Mn_{20}Co_8$ alloys have nearly identical γ-phase behavior, while the $Fe_{76}Mn_{19}Co_5$ alloy has the lowest amount of γ in the undeformed condition. The only alloy which does not exhibit any degree of α' transformation is the equiatomic alloy. Otherwise, the α'-phase displays a reverse trend to the ε-phase, indicating $\varepsilon \rightarrow \alpha'$ transformation. This chain will be discussed in greater detail in chapter 5.1.

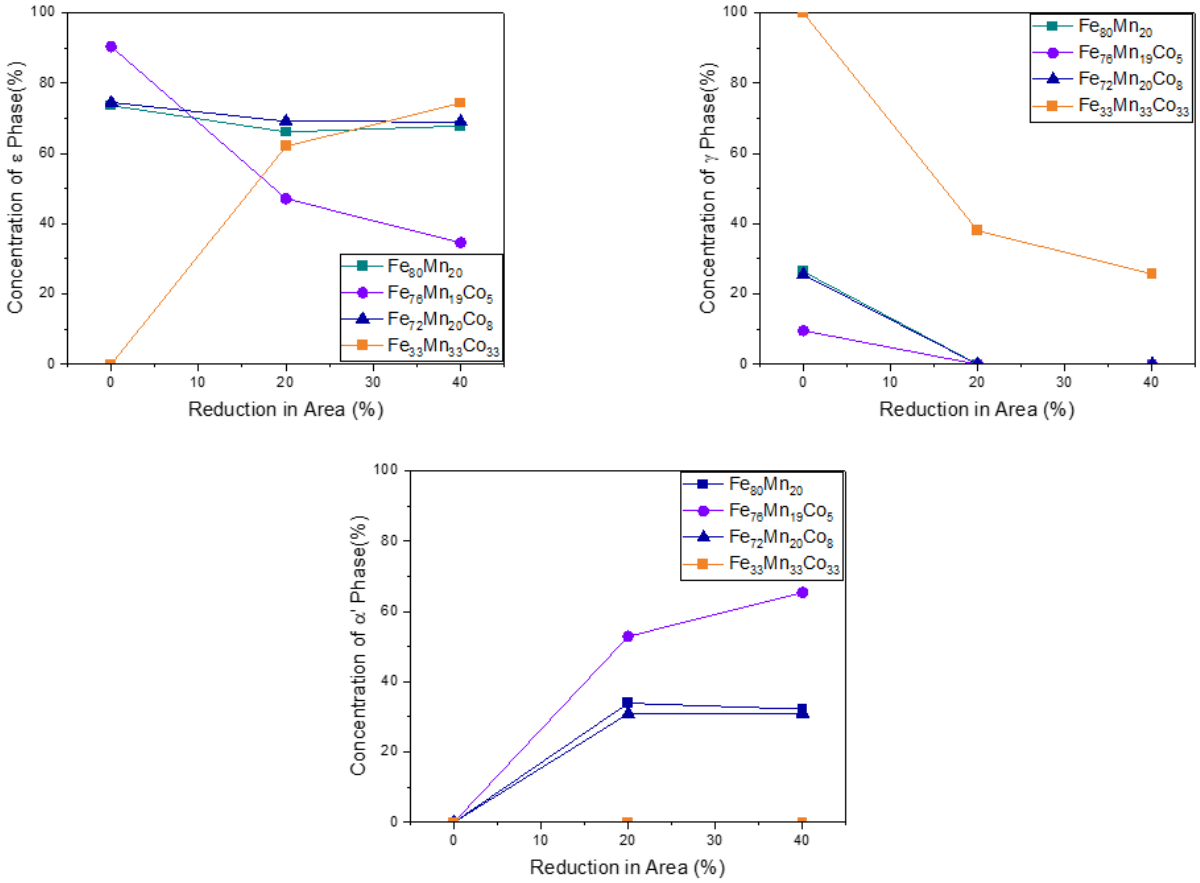

Figure 4.7: Phase constitution as a function of % reduction of area due to cold work for the (a) ε-phase, (b) γ-phase, and (c) α'-phase.

4.3 Scanning Electron Microscopy

The SEM was used to examine local deformation events at high resolution and provide additional insight into their mechanisms via EBSD analysis. Microhardness indents were made to induce deformation and scans were completed along the periphery of the indents. Characteristic images of each alloy are shown here.

Figure 4.8 shows a BSE image of a microhardness indent in the $Fe_{80}Mn_{20}$ alloy with a corresponding phase map (PM) and inverse pole figure (IPF) to the right.

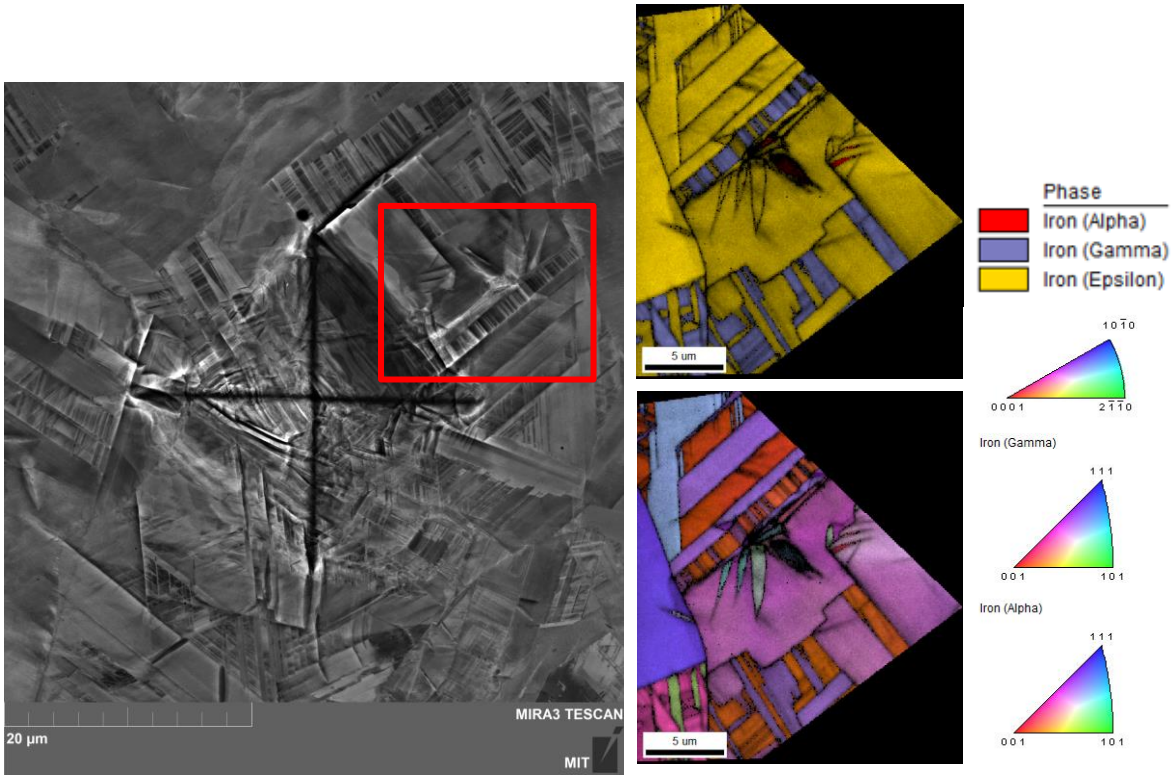

Figure 4.8: *(Left):* BSE image of a microhardness indent in the $Fe_{80}Mn_{20}$ alloy. Red area is shown in an EBSD (*top right):* phase map and *(bottom right):* inverse pole figure.

Small amounts of α' phase can be seen within existing HCP plates. Additionally, several fingers of different orientation within the HCP plate are observed in the IPF and PM. A misorientation trace was completed across the fingers to check for evidence of twinning. Figure 4.9 shows a twin parent-daughter map with the misorientation profile taken across the regions of misorientation.

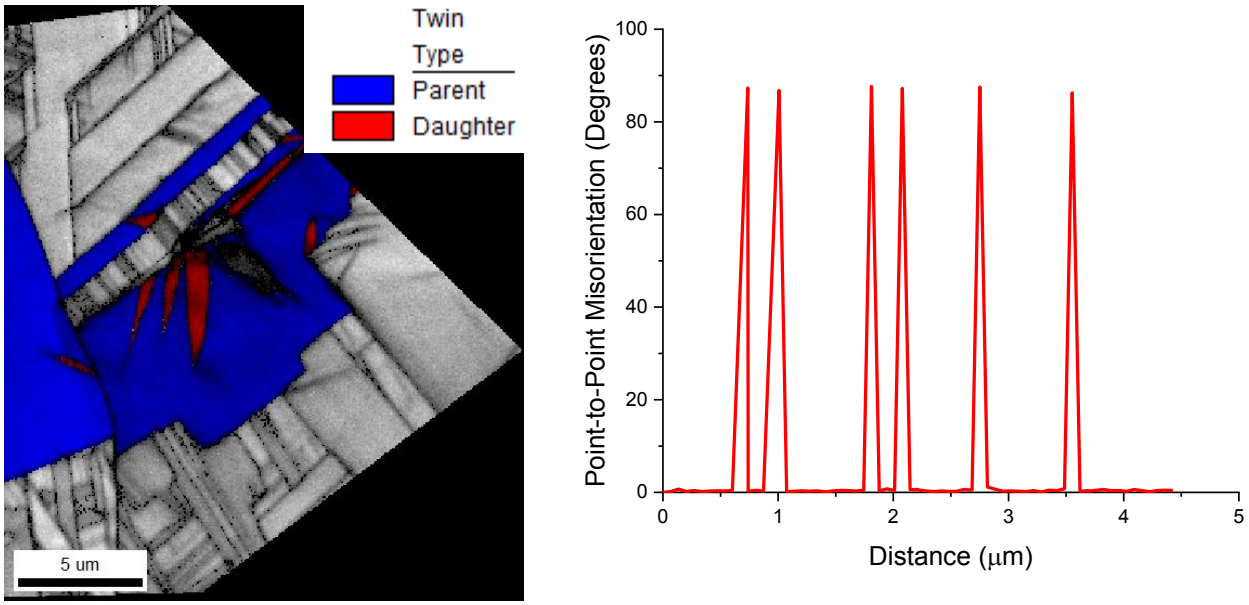

Figure 4.9: *(Left):* Twin parent-daughter map of region near microhardness indent in $Fe_{80}Mn_{20}$ alloy. Parent grains are shown in blue while regions of twinning are given in red. *(Right)*: Misorientation profile for regions of misorientation shown by white line in parent-daughter map.

The misorientation angle was measured at 87.13°. They are thought to be twins of $\{10\bar{1}2\} < \bar{1}011 >$, a common type of HCP twin [46,47]. Based on the c/a ratio of 1.61350, this type of twin would be classified as an extension twin [47].

Figure 4.10 shows a BSE image of a microhardness indent in the $Fe_{76}Mn_{19}Co_5$ alloy with a corresponding phase map (PM) and inverse pole figure (IPF) to the right.

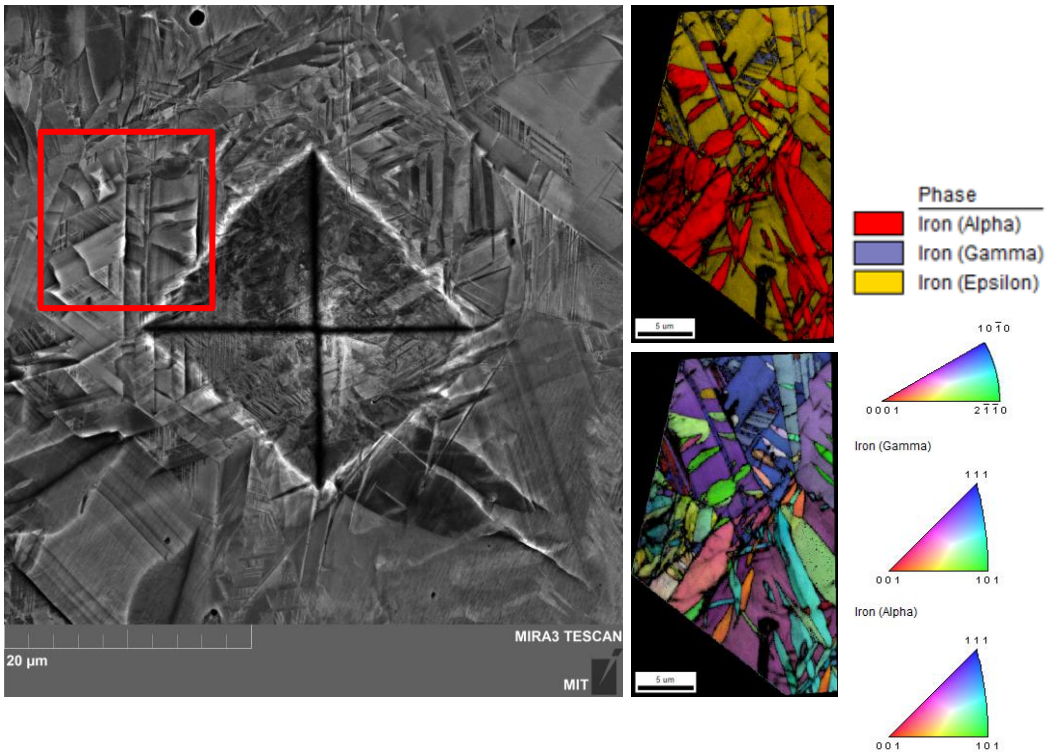

Figure 4.10: *(Left):* BSE image of a microhardness indent in the $Fe_{76}Mn_{19}Co_5$ alloy. Red area is shown in an EBSD (*top right):* phase map and *(bottom right):* inverse pole figure.

A high amount of α' is seen and very little γ remains. While there is no visible evidence of twinning in the ε or γ-phases, the α'-phase may have twin systems. The α' twin system is $\{112\} < 111 >$ [48]. As can be seen from the IPF in Figure 4.10, the α'-phase shows a great degree of difference in orientation. This misorientation may be the result of deformation twinning or because individual grains of differing orientation are nucleated. Though time prohibited a deeper exploration of these phenomena, the nature of α' crystallographic nature is an excellent candidate for future study and characterization. The small grain size of α' should also be noted as it would be expected to play a significant role in the strain hardening behavior of the material. The large amount of α' formation has several possible mechanisms which will be discussed in greater detail in chapter 5.1.

Figure 4.11 shows a BSE image of a microhardness indent in the $Fe_{72}Mn_{20}Co_8$ alloy with a corresponding phase map (PM) and inverse pole figure (IPF) to the right.

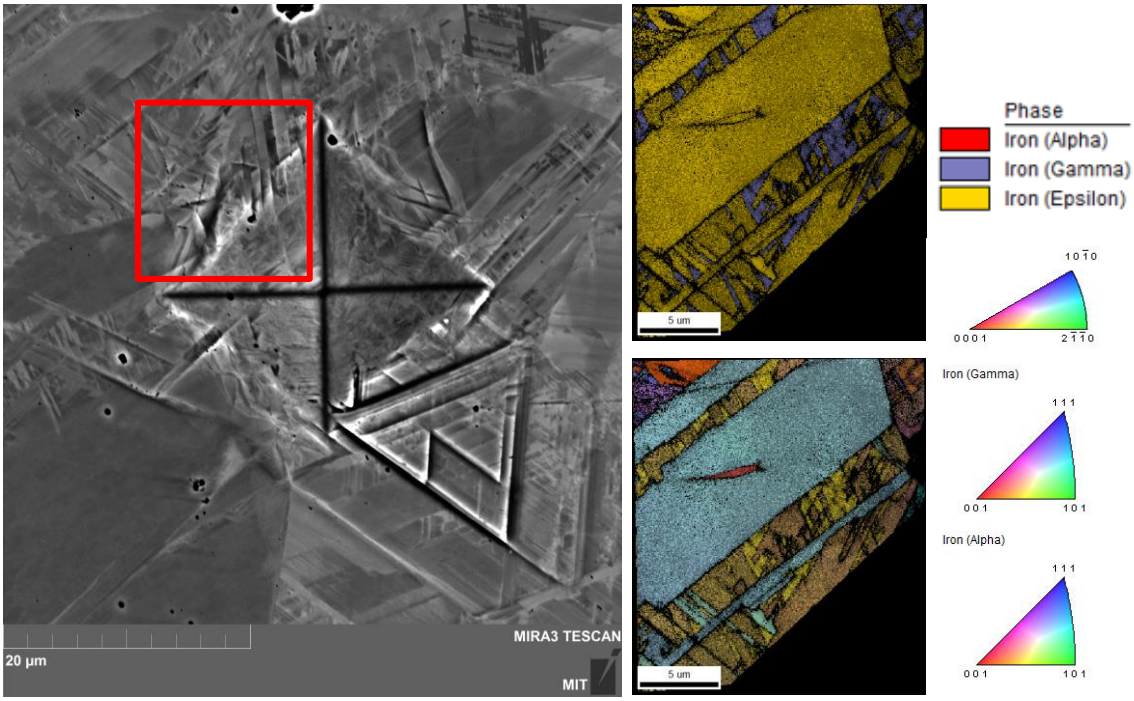

Figure 4.11: *(Left):* BSE image of a microhardness indent in the $Fe_{72}Mn_{20}Co_8$ alloy. Red area is shown in an EBSD (*top right):* phase map and *(bottom right):* inverse pole figure.

The region is mostly ε-phase with traces of γ present. There is no evidence of α' formation within either of the other two phases. A single region within the HCP phase shows misorientation that could be a candidate for twinning. Figure 4.12 shows a twin parent-daughter map with the misorientation profile taken across the region of misorientation.

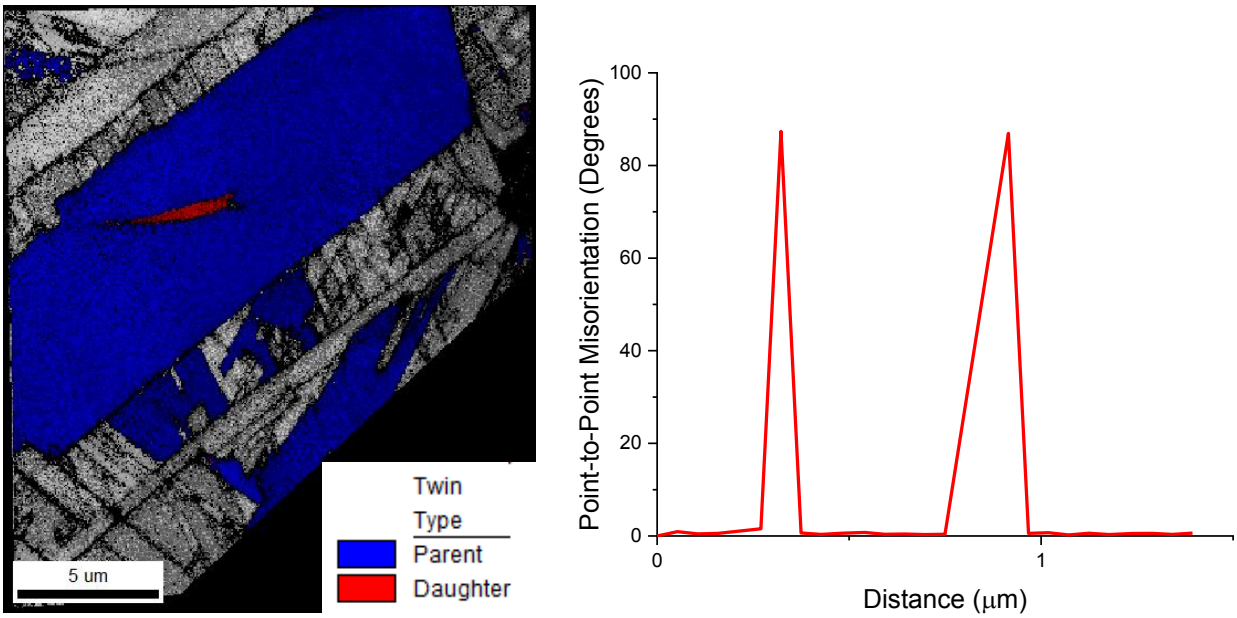

Figure 4.12: *(Left):* Twin parent-daughter map of region near microhardness indent in $Fe_{80}Mn_{20}$ alloy. Parent grains are shown in blue while regions of twinning are given in red. *(Right)*: Misorientation profile for regions of misorientation shown by white line in parent-daughter map.

The misorientation angle was measured at 87.15°. They are thought to be twins of $\{10\bar{1}2\} < \bar{1}011 >$, a common type of HCP twin [46,47]. Based on the c/a ratio of 1.61350, this type of twin would be classified as an extension twin [47].

Figure 4.13 shows a BSE image of a microhardness indent in the $Fe_{33}Mn_{33}Co_{33}$ alloy with a corresponding phase map (PM) and inverse pole figure (IPF) to the right.

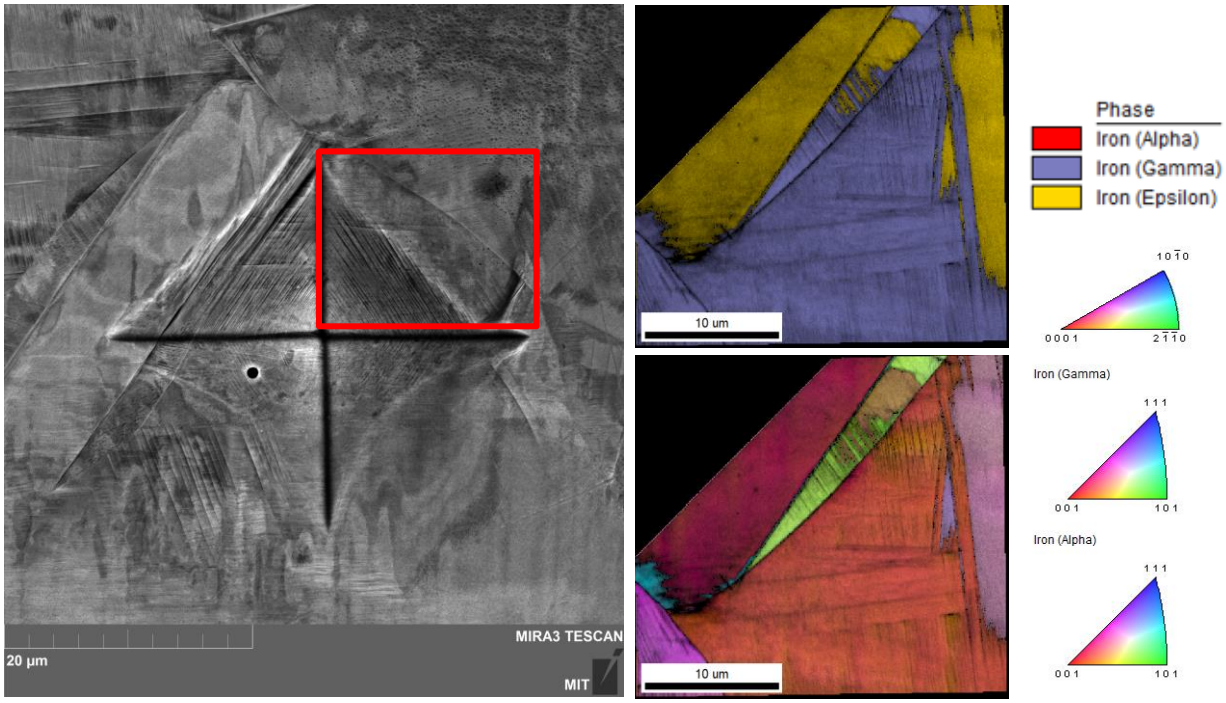

Figure 4.13: *(Left):* BSE image of a microhardness indent in the $Fe_{33}Mn_{33}Co_{33}$ alloy. Red area is shown in an EBSD (*top right):* phase map and *(bottom right):* inverse pole figure.

The region shows larger amounts of γ as expected from the XRD results, with packets of ε appearing close to the areas of deformation. No evidence of twinning was seen in this alloy, nor was any trace of α' found. These findings suggest and support the XRD data that the dominant deformation mechanism of the FCC γ-phase is martensitic transformation to the HCP ε-phase.

4.4 Microhardness Testing

Vickers microhardness testing was completed as described in chapter 2.4.1 as a means to evaluate the mechanical properties of each alloy at different stages of deformation to estimate the strain hardening capability of each alloy. A change in hardness can correlate to phase transformation, twinning, dislocation pileups, or a combination of the three. Certain effects may cause stress relief during deformation which could cause a reduction in hardness [7, 19-21,48]. Hardness results are shown vs. % reduction in thickness as a result of cold working in Figure 4.15 for each alloy in the study.

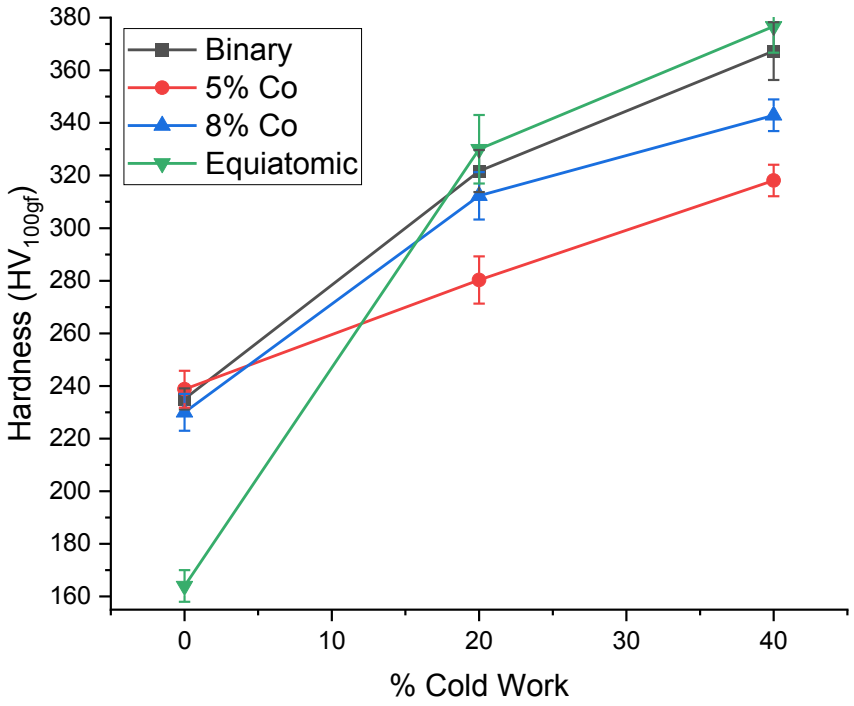

Figure 4.14: Vickers microhardness vs. % reduction in thickness from cold working for each alloy in the study.

The $Fe_{80}Mn_{20}$ alloy experiences a high strain hardening rate from 0 to 20% reduction in thickness, and then a less steep increase in hardness until 40% reduction in thickness. The $Fe_{76}Mn_{19}Co_5$ and $Fe_{72}Mn_{20}Co_8$ alloys both exhibit lower hardness than the binary system, though the alloy with 8% Co alloy is harder than the one with 5% Co. The $Fe_{33}Mn_{33}Co_{33}$ alloy shows massive strain hardening. These results will be analyzed and discussed in greater detail in chapter 5.1. The hardness results are summarized in tabular form in Table 4.6.

Table 4.6: Summary of microhardness results for each alloy.

Alloy Composition	Undeformed Hardness (HV)	20% CR Hardness (HV)	40% CR Hardness
$Fe_{80}Mn_{20}$	235.1 ± 4	321.7 ± 8	367.3 ± 11
$Fe_{79}Mn_{19}Co_5$	238.8 ± 7	280.3 ± 9	318.1 ± 6
$Fe_{72}Mn_{20}Co_8$	230.0 ± 6	312.3 ± 15	342.9 ± 10
$Fe_{33}Mn_{33}Co_{33}$	164 ± 6	330 ± 13	376.7 ± 10

THIS PAGE INTENTIONALLY LEFT BLANK

Chapter 5

Discussion and Conclusions

This study sought to examine the effects of Co when systematically added to the Fe-Mn system. Four alloys were produced using predicted thermodynamic properties as their basis and several tests ran to evaluate the results experimentally. A discussion of the theoretical calculations in chapter 3 and the experimental results in chapter 4 will take place here by examining the results obtained for each alloy holistically.

5.1 Discussion of Results

Using the model developed in chapter 3, the binary $Fe_{80}Mn_{20}$ alloy has a predicted SFE of 7.0 mJ/m^2. The low, slightly positive stacking fault energy is expected to result in the preferred deformation mechanism of the FCC γ-phase being martensitic transformation to the HCP ε-phase [10]. As observed in the XRD data, however, the ε-phase also slightly diminishes with deformation and the formation of BCT α' phase is observed. These results are expected, as literature reports that Fe-Mn alloys with Mn contents beneath 23 at. % produce α' during deformation [6,7]. The ε-phase is also known to be an intermediate phase in the transformation of $\gamma \rightarrow \alpha'$ and the transformation is explained by classic Bain correspondence [20]. SEM data visually shows α' within HCP plates near microhardness indentations and also evidence of twinning, indicating SFE which is relatively low but still high enough to lead to mixed modes of deformation [13]. The rise in hardness with deformation is expected, especially with the large amounts of martensite formation observed.

As Co is added to the system in the $Fe_{76}Mn_{19}Co_5$ alloy, the response to deformation changes. The predicted SFE of 12.9 mJ/m^2 would seem to indicate that martensitic transformation is still favorable, but perhaps with some twinning in both the FCC and HCP phases. However, no twinning is observed in either of these phases in this alloy and a substantial decrease in ε-phase is measured from XRD during deformation. A large degree of α' phase forms initially and continues to increase, though its rate of formation is substantially lower between 20% and 40% reduction in thickness than between 0% and 20% reduction in thickness. There are several possible explanations for the mechanism of α' formation.

One possible explanation is that the addition of Co helps to develop the ability of the material to facilitate plastic accommodation during deformation [35, 37]. A phenomenon known as the Suzuki window effect is one such explanation but seems unlikely as the α' phase forms in regions other than the intersection of HCP ε bands. Formation of α' along shear band intersection and in regions of overlapping stacking faults is more likely [12,50,51]. This would indicate that Co has an effect not only on the SFE and stability and behavior of the γ-phase, but also on the ε-phase [12,50,51]. SEM imagery shows a high amount of α' in the immediate

vicinity of microhardness indents, supporting the phase composition data provided by XRD. Despite the high concentration of both α' and ε martensite after deformation, however, the $Fe_{76}Mn_{19}Co_5$ alloy had the lowest hardness after deformation. This result could be due to a strain accommodation affect through formation of α', but may also be because of accommodation from the twin variants formed through deformation [48]. A higher degree of twin formation, even in the BCT phase, is supported by the predicted increase in SFE [50]. Twins in BCT structures usually occur as the result of shear mechanisms and literature regarding twins of this nature seem to support that the primary mechanism of twin formation observed here is shear [46, 48].

With higher Co concentration, as in the $Fe_{72}Mn_{20}Co_8$ alloy, predicted SFE further increases to 18.1 mJ/m^2. Martensitic transformation of γ-phase to ε-phase should diminish, and twinning and slip should become to dominant mode of deformation of γ. The XRD data supports this prediction well, as there is virtually no change in the concentration of ε observed throughout deformation. Additionally, the higher amount of Co has a stabilizing effect on the HCP ε-phase. The parent γ-phase instead transforms to α' from 0% to 20% reduction in thickness, and then both phases remain fairly constant from 20% to 40%. There is some evidence of twinning within the HCP as well. Given the $\{10\bar{1}2\} < \bar{1}011 >$ nature of the extension twin, this deformation is likely caused by a combination of shear and shuffle methods [46]. The higher hardness observed in comparison to the $Fe_{76}Mn_{19}Co_5$ alloy can be attributed to the lack of window effect observed in this alloy as also evidenced by XRD results and SEM imagery.

When the Fe:Mn ratio of 4:1 is no longer observed as in the equiatomic $Fe_{33}Mn_{33}Co_{33}$ alloy, behavior changes significantly. The high predicted SFE of 94.1 mJ/m^2 would lead to an expected deformation mode solely of dislocation slip. However, experimental results contradict this prediction. XRD results indicate that what starts as a purely γ-phase microstructure transforms into ε-phase as deformation commences. SEM imagery supports this finding, as a significant amount of ε-phase within a γ-phase matrix is observed near microhardness indentations. The low hardness of the undeformed material is attributed to the pure γ-phase microstructure in this condition. The high levels of strain hardening observed are explained by martensitic transformation and the absence of any means of plastic accommodation. The absence of α' supports the finding that no accommodation is occuring. Higher deformed hardness than the other alloys which showed α' formation also supports this theory. The shape of the line showing the increase in ε-phase in Figure 4.6d with increasing deformation correlates very well with the shape of the line showing the increase in hardness shown in Figure 4.14, indicating that martensitic transformation is the primary method of hardening in this alloy.

5.2 Conclusions

This study sought to examine the effect of Co on the deformation response of Fe-Mn alloys. The following conclusions can be drawn from the data generated in this study:

1. According to the thermodynamic model used in the study, Co increases the SFE of Fe-Mn alloys when added to alloys with a fixed Fe:Mn ratio of 4. Using the regular/sub-regular solution model with up-to-date parameters and an improved magnetic model used by the CALPHAD community, this model can be used for the Fe-Mn-Co system with low levels of Co and show reasonable agreement with experimental data. As the system approaches equiatomic concentrations, the model breaks down and strays away from expected results.

2. Small additions of Co (below 8 at. %) seem to enhance the $\varepsilon \rightarrow \alpha'$ transformation compared to the binary system. The addition of some amount of Co seems to aid in thermal ε formation as shown in the starting phase constitution of the 5 at. % Co alloy shown in Figure 4.6. This finding is in line with expectations from the HCP nature of elemental Co [40]. Alloys with lower additions of Co are predicted to have a lower SFE and therefore support overlap of stacking faults and the formation of ε-phase [12,50,51], the combination of which form ideal nucleation sites for α'.

3. Above 8 at. % Co, the HCP ε-phase appears to be mechanically stabilized as virtually no change in ε concentration was observed up to 40% reduction in thickness due to cold work. The increased mechanical stability of the ε-phase could be intuitively predicted by the addition of Co [40], but additionally the predicted rise in SFE would make stacking fault overlap more irregular and require α' formation at shear band intersection. The combination of these effects would reduce deformation induced α' formation.

4. The $Fe_{76}Mn_{19}Co_5$ alloy exhibits the lowest hardness and hardenability. Alloys which show greater $\varepsilon \rightarrow \alpha'$ transformation have lower hardness and hardenability than alloys which experience $\gamma \rightarrow \alpha'$ transformation or no α' transformation. It is believed that some mechanism of plastic accommodation or deformation twinning is the reason for the lower hardness despite the higher amounts of α' formation.

5.3 Future Work and Recommendations

Further study on the effect of Co in the Fe-Mn system is desirable for advancement in alloy design of these materials. In particular, the following suggestions are made:

1. Deeper exploration into the thermodynamic model developed for these alloys. Though this study shows reasonable agreement with literature and experimental data at low Co concentrations, the deviation between behavior predicted from calculated theoretical results and observed experimental data is substantial for the alloy of equiatomic composition. It is unclear where this breakdown occurs in the model, if it is the only breakdown, and what causes the breakdown. Several authors note the lack of experimental data in the Fe-Mn-Co ternary system [41-43] and a richer understanding of the behavior of the ternary system across compositional ranges would be useful for future alloy design. Specifically, a greater amount of experimental data should be used to develop more accurate models for T_C^{ϕ}.

2. Testing at smaller compositional step sizes. Since the change in behavior from 5 to 8 at. % Co is so significant, a precise look at where the change in behavior takes place is needed to determine where the transition from enhanced window effect to very stable ε-phase takes place.

3. Testing at smaller cold working reduction in thickness step sizes. Strain hardenability changes with the severity of deformation, and more data between 20% and 40% and exceeding 40% reduction in thickness would be useful in determining where these transitions occur.

4. Exploring the effect of Co with differing Fe:Mn ratios. Higher Mn concentrations have the effect of stabilizing the γ-phase and may in turn yield different results than the 4:1 ratio used in this study.

5. Tensile testing should be completed to obtain accurate data on the mechanical properties of the alloys studied. As the intended applications of these alloys are likely structural in nature, a precise definition of these properties would be useful in assessing the capabilities of these alloys.

6. Addition of Cr. Though this is a fundamental study on the effects of Co on the Fe-Mn system, the feasibility of these alloys for engineering use is limited due to poor corrosion resistance. While Cr addition will not enrich the current study, it is another step that should be taken to evaluate the overall engineering performance of Mn-Co steels.

7. Further exploration of the crystallography of observed transformation chains. Specifically, the nature of twinning within the α' and ε-phases and the crystallography regarding the $\varepsilon \rightarrow \alpha'$ martensitic transformation could be further enriched. WLR theory would be a useful tool in defining and predicting habit planes, misorientation, and shear required for transformation [49].

Acknowledgements

I would like to thank my advisor Dr. Cem Tasan and my student mentor Shaolou Wei for their continued expertise, guidance, and patience throughout the course of this research. Their vision, knowledge, creativity, and work ethic are second to none and I am very grateful for the opportunity to learn even a small fraction of what they know. Additionally, I would like to thank my fellow lab members in the Tasan Group. This work was completed during the worldwide pandemic of COVID-19 and without their advice, training, and welcoming nature this work would not have been possible.

I would also like to thank the laboratory managers in the Department of Materials Science & Engineering at MIT. Dr. Charles Settens was always readily available despite the pandemic and provided quick training and expert advice for the XRD experiments which formed the basis for much of this work. Dr. Shaymus Hudson provided a huge amount of knowledge with regards to sample preparation and processing and has knowledge far beyond his tears. Dr. Mike Tarkanian was instrumental in the production of alloys created for this study and ensured safe usage of all equipment even in experiments which involved a degree of risk. All three maintain their facilities in world-class condition and are a major contributing factor in the high esteem with which the department is held worldwide.

Furthermore, I would like to thank my classmates and mentors in the Navy's 2N program. Every one of you was in part responsible for my success here and I am proud to have been able to work with you in some capacity. I hope to see you all again someday! Fair winds and following seas!

Finally, I would like to thank my friends and family who saw me through a very difficult three years of graduate education. I would especially like to thank my fiancé Kirsten and soon to be stepson Kellan. You both made all the late nights, work anxiety, and self-doubt more tolerable and I can't wait to see what comes next for us.

THIS PAGE INTENTIONALLY LEFT BLANK

References

[1] P. Chowdhury, D. Canadinc, and H. Sehitoglu, “On deformation behavior of Fe-Mn based structural alloys,” *Mater. Sci. Eng. R Reports*, vol. 122, pp. 1–28, 2017, doi: 10.1016/j.mser.2017.09.002.

[2] Z. F. He, N. Jia, H. W. Wang, Y. Liu, D. Y. Li, and Y. F. Shen, “The effect of strain rate on mechanical properties and microstructure of a metastable FeMnCoCr high entropy alloy,” *Mater. Sci. Eng. A*, vol. 776, no. November 2019, 2020, doi: 10.1016/j.msea.2020.138982.

[3] J. H. Jun and C. S. Choi, “Effect of Si and Co addition on the microstructure of Fe-Mn alloy,” *J. Mater. Sci. Lett.*, vol. 17, no. 8, pp. 629–631, 1998, doi: 10.1023/A:1006699602782.

[4] W. Lu, C. H. Liebscher, G. Dehm, D. Raabe, and Z. Li, “Bidirectional Transformation Enables Hierarchical Nanolaminate Dual-Phase High-Entropy Alloys,” *Adv. Mater.*, vol. 30, no. 44, pp. 1–10, 2018, doi: 10.1002/adma.201804727.

[5] S. Wei, J. Kim, J. L. Cann, R. Gholizadeh, N. Tsuji, and C. C. Tasan, “Plastic strain-induced sequential martensitic transformation,” *Scr. Mater.*, vol. 185, pp. 36–41, 2020, doi: 10.1016/j.scriptamat.2020.03.060.

[6] S. Wei, M. Jiang, and C. C. Tasan, “Interstitial-Free Bake Hardening Realized by Epsilon Martensite Reverse Transformation,” *Metall. Mater. Trans. A Phys. Metall. Mater. Sci.*, vol. 50, no. 9, pp. 3985–3991, 2019, doi: 10.1007/s11661-019-05344-4.

[7] J. Su, X. Wu, D. Raabe, and Z. Li, “Deformation-driven bidirectional transformation promotes bulk nanostructure formation in a metastable interstitial high entropy alloy,” *Acta Mater.*, vol. 167, pp. 23–39, 2019, doi: 10.1016/j.actamat.2019.01.030.

[8] J. Chen, J. Sun, Q. Yang, H. Peng, S. Wang, and Y. Wen, “Thermodynamic Explanation for the Large Difference in Improving Shape Memory Effect of Fe–Mn Alloys by Co and Si Addition,” *Adv. Eng. Mater.*, vol. 18, no. 8, pp. 1426–1433, 2016, doi: 10.1002/adem.201500645.

[9] E. R. Parker and V. F. Zackay, “Enhancement of fracture toughness in high strength steel by microstructural control,” *Eng. Fract. Mech.*, vol. 5, no. 1, pp. 147–165, 1973, doi: 10.1016/0013-7944(73)90013-1.

[10] Y. Li, W. Li, J. C. Hu, H. M. Song, and X. J. Jin, “Compatible strain evolution in two phases due to epsilon martensite transformation in duplex TRIP-assisted stainless steels with high hydrogen embrittlement resistance,” *Int. J. Plast.*, vol. 88, pp. 53–69, 2017, doi: 10.1016/j.ijplas.2016.09.012.

[11] T. Wang *et al.*, “Co-introduction of precipitate hardening and TRIP in a TWIP high-entropy alloy using friction stir alloying,” *Sci. Rep.*, vol. 11, no. 1, pp. 1–10, 2021, doi: 10.1038/s41598-021-81350-0.

[12] G. B. Olson and M. Cohen, “A general mechanism of martensitic nucleation: Part I. General concepts and the FCC→HCP transformation,” *Metall. Trans. A*, vol. 7, no. 11, pp. 1897–1904, 1976, doi: 10.1007/BF02654987.

[13] L. Remy and A. Pineau, “Twinning and strain-induced F.C.C. → H.C.P. transformation in the FeMnCrC system,” *Mater. Sci. Eng.*, vol. 28, no. 1, pp. 99–107, 1977, doi: 10.1016/0025-5416(77)90093-3.
[14] Holden, A., Bolton, J. D. & Petty, E. R. Alloys, Structure and Properties of Iron-Manganese. J. Iron Steel Inst. 721–728 (1971).
[15] Y. Tomota, M. Strum, and J. W. Morris, “Microstructural dependence of Fe-high Mn tensile behavior,” Metall. Trans. A, vol. 17, no. 3, pp. 537–547, 1986, doi: 10.1007/BF02643961.
[16] A. A. H. Hamers and C. M. Wayman, “Shape memory behavior in FeMnCo alloys,” *Scr. Metall. Mater.*, vol. 25, no. 12, pp. 2723–2728, 1991, doi: 10.1016/0956-716X(91)90146-R.
[17] A. Borgenstam and M. Hillert, “Driving Force for FCC -> BCC Martensites in Fe-X Alloys,” *Acta Mater.*, vol. 45, no. 5, pp. 2079–2091, 1997.
[18] X. S. Yang, S. Sun, H. H. Ruan, S. Q. Shi, and T. Y. Zhang, “Shear and shuffling accomplishing polymorphic fcc γ → hcp ε → bct α martensitic phase transformation,” *Acta Mater.*, vol. 136, no. July, pp. 347–354, 2017, doi: 10.1016/j.actamat.2017.07.016.
[19] T. Suzuki, H. Kojima, K. Suzuki, T. Hashimoto, and M. Ichihara, “An experimental study of the martensite nucleation and growth in 18/8 stainless steel,” *Acta Metall.*, vol. 25, no. 10, pp. 1151–1162, 1977, doi: 10.1016/0001-6160(77)90202-4.
[20] R. L. Grunes, C. D’Antonio, and K. Mukherjee, “A study of α′ martensite nucleation in the iron15% Mn alloy,” *Mater. Sci. Eng.*, vol. 9, no. C, pp. 1–6, 1972, doi: 10.1016/0025-5416(72)90003-1.
[21] T. Ogawa, M. Koyama, C. C. Tasan, K. Tsuzaki, and H. Noguchi, “Effects of martensitic transformability and dynamic strain age hardenability on plasticity in metastable austenitic steels containing carbon,” *J. Mater. Sci.*, vol. 52, no. 13, pp. 7868–7882, 2017, doi: 10.1007/s10853-017-1052-3.
[22] M. Matsui, K. Sato, and K. Adachi, “Magnetic Properties of FCC γ-phase in the Ternary Co-Mn-Fe System,” *J. Phys. Soc. Japan*, vol. 35, no. 2, pp. 419–425, 1973.
[23] O. A. Khomenko, I. F. Khil’kevich, and G. Y. Zviginstseva, “Influence of a Third Component on the Neel Point of Iron Manganese Invariables,” *Phys. Met. Metallogr.*, vol. 37, no. 6, pp. 186–188, 1974.
[24] L. Reimer, *Scanning Electron Microscopy*, 2nd ed. New York: Springer-Verlag Berlin Heidelberg, 2005.
[25] B. E. Warren, *X-Ray Diffraction*. Dover Publications, 1990.
[26] B. Fultz, *Phase Transitions in Materials*. Cambridge University Press, 2020.
[27] D. T. Pierce, J. A. Jiménez, J. Bentley, D. Raabe, C. Oskay, and J. E. Wittig, “The influence of manganese content on the ha fault and austenite/ε-martensite interfacial energies in Fe-Mn-(Al-Si) steels investigated by experiment and theory,” *Acta Mater.*, vol. 68, pp. 238–253, 2014, doi: 10.1016/j.actamat.2014.01.001.
[28] Y. K. Lee and C.-S. Choi, “Driving Force for γ→ε Martensitic Transformation and Stacking Fault Energy of γ in Fe-Mn Binary System,” *Metall. Mater. Trans. A*, vol. 31A, no. February, pp. 355–360, 2000.

[29] P. Marinelli, M. Sade, and A. Fernández Guillermet, “On the structural changes accompanying the fcc/hcp martensitic transformation in Fe-Mn-Co alloys,” *Scr. Mater.*, vol. 46, no. 11, pp. 805–810, 2002, doi: 10.1016/S1359-6462(02)00080-5.
[30] A. T. Dinsdale, “SGTE DATA FOR PURE ELEMENTS A T Dinsdale Division of Materials Metrology, National Physical Laboratory, Teddington, Middlesex, TWl 1 OLW, UK,” *Calphad*, vol. 15, no. 4, pp. 317–425, 1991.
[31] J. Wang, X.-G. Lu, N. Zhu, and W. Zheng, “Thermodynamic and Diffiusion Kinetic Studies of the Fe-Co System,” *Calphad Comput. Coupling Phase Diagrams Thermochem.*, vol. 58C, pp. 82–100, 2017, doi: https://doi.org/10.1016/j.calphad.2017.06.001.
[32] W. Huang, “An Assessment of the Co-Mn System,” *CALPHAD*, vol. 13, no. 3, pp. 231–242, 1989.
[33] M. Hillert and M. Jarl, “A Model for Alloying Effects in Ferromagnetic Metals,” *CALPHAD*, vol. 2, no. 3, pp. 227–238, 1978.
[34] G. Inden, “The Role of Magnetism in the Calculation of Phase Diagrams,” *Phys. B + C*, vol. 103, no. 1, pp. 82–100, 1981.
[35] K. J. Tauer and R. J. Weiss, “Magnetic Second-Order Transitions E ;,” 1955.
[36] W. Xiong, Q. Chen, P. A. Korzhavyi, and M. Selleby, “An improved magnetic model for thermodynamic modeling,” *Calphad Comput. Coupling Phase Diagrams Thermochem.*, vol. 39, pp. 11–20, 2012, doi: 10.1016/j.calphad.2012.07.002.
[37] W. Huang, “Thermodynamics of the Co-Fe-Mn System,” *CALPHAD*, vol. 14, no. 1, pp. 11–22, 1990.
[38] S. Lu, Q. M. Hu, B. Johansson, and L. Vitos, “Stacking fault energies of Mn, Co and Nb alloyed austenitic stainless steels,” *Acta Mater.*, vol. 59, no. 14, pp. 5728–5734, 2011, doi: 10.1016/j.actamat.2011.05.049.
[39] S. F. Liu *et al.*, “Stacking fault energy of face-centered-cubic high entropy alloys,” *Intermetallics*, vol. 93, no. October, pp. 269–273, 2018, doi: 10.1016/j.intermet.2017.10.004.
[40] C.-S. Yoo, P. Söderlind, and H. Cynn, “The phase diagram of cobalt at high pressure and temperature: the stability of -cobalt and new -cobalt,” *J. Phys. Condens. Matter*, vol. 10, no. 20, pp. L311–L318, 1998, doi: 10.1088/0953-8984/10/20/001.
[41] P. La Roca, P. Marinelli, A. Baruj, M. Sade, and A. Fernández Guillermet, “Composition dependence of the Néel temperature and the entropy of the magnetic transition in the fcc phase of Fe-Mn and Fe-Mn-Co alloys,” *J. Alloys Compd.*, vol. 688, pp. 594–598, 2016, doi: 10.1016/j.jallcom.2016.07.213.
[42] A. L. Baruj, “Transformación Martensítica , Estabilidad Relativa de Fases fcc y hcp , y Efectos del Ciclado Térmico en Aleaciones Fe-Mn y Fe-Mn-X (X = Co , Si),” 1999.
[43] P. Marinelli, A. Fernández Guillermet, and M. Sade, “The enthalpy change of the hcp → fcc martensitic transformation in Fe-Mn-Co alloys: Composition dependence and thermal cycling effects,” *Mater. Sci. Eng. A*, vol. 373, no. 1–2, pp. 1–9, 2004, doi: 10.1016/j.msea.2003.05.006.

[44] S. Bigdeli and M. Selleby, “A Thermodynamic Assessment of the Binary Fe-Mn System for the Third Generation of CALPHAD Databases,” *Calphad Comput. Coupling Phase Diagrams Thermochem.*, vol. 64, pp. 185–195, 2019, doi: https://doi.org/10.1016/j.calphad.2018.11.011.
[45] M. Palumbo, “Thermodynamics of martensitic transformations in the framework of the CALPHAD approach,” *Calphad Comput. Coupling Phase Diagrams Thermochem.*, vol. 32, no. 4, pp. 693–708, 2008, doi: 10.1016/j.calphad.2008.08.006.
[46] P. Partridge, “The crystallography and deformation modes of hexagonal close-packed metals,” pp. 169–194.
[47] M. Hyong Yoo and C. T. Wei, “Growth of deformation twins in zinc crystals,” *Philos. Mag.*, vol. 14, no. 129, pp. 573–587, 1966, doi: 10.1080/14786436608211952.
[48] S. Mahajan, “FORMATION AND ACCOMMODATION AT DEFORMATION TWINS IN bcc CRYSTALS.,” vol. 12, no. March, pp. 225–235, 1982.
[49] M. S. Wechsler, D. S. Lieberman, and T. A. Read, “On the theory of the formation of martensite,” *Trans. AIME*, vol. 197, no. November, pp. 1503–1515, 1953, [Online]. Available: http://www.scopus.com/inward/record.url?eid=2-s2.0-0001483635&partnerID=tZOtx3y1.
[50] Y. Tian, O. I. Gorbatov, A. Borgenstam, A. V. Ruban, and P. Hedström, “Deformation Microstructure and Deformation-Induced Martensite in Austenitic Fe-Cr-Ni Alloys Depending on Stacking Fault Energy,” *Metall. Mater. Trans. A Phys. Metall. Mater. Sci.*, vol. 48, no. 1, pp. 1–7, 2017, doi: 10.1007/s11661-016-3839-2.
[51] J. Talonen and H. Hänninen, “Formation of shear bands and strain-induced martensite during plastic deformation of metastable austenitic stainless steels,” *Acta Mater.*, vol. 55, no. 18, pp. 6108–6118, 2007, doi: 10.1016/j.actamat.2007.07.015.